

A MEASUREMENT OF THE  $W\gamma$  CROSS SECTION AT  $\sqrt{S} = 8$  TEV IN  $PP$   
COLLISIONS WITH THE CMS DETECTOR

by

Ekaterina Avdeeva

A DISSERTATION

Presented to the Faculty of  
The Graduate College at the University of Nebraska  
In Partial Fulfilment of Requirements  
For the Degree of Doctor of Philosophy

Major: Physics & Astronomy

Under the Supervision of Professor Ilya Kravchenko

Lincoln, Nebraska

May, 2017

A MEASUREMENT OF THE  $W\gamma$  CROSS SECTION AT  $\sqrt{S} = 8$  TEV IN  $PP$   
COLLISIONS WITH THE CMS DETECTOR

Ekaterina Avdeeva, Ph.D.

University of Nebraska, 2017

Adviser: Someone

Abstract goes here.

# Contents

<b>Contents</b>	<b>iii</b>
<b>1 Introduction</b>	<b>1</b>
1.1 Fundamental Particles and Interactions . . . . .	4
1.2 Electroweak Interactions . . . . .	8
1.3 Strong Interactions . . . . .	13
1.4 Physics of Proton-Proton Collisions . . . . .	15
1.5 Open Questions of the Standard Model . . . . .	17
<b>2 <math>W\gamma</math> Production Theory and Former Experimental Results</b>	<b>19</b>
2.1 Electroweak Theory of the Standard Model . . . . .	20
2.2 Cross Section and Luminosity . . . . .	29
2.3 Standard Model $W\gamma$ Production . . . . .	32
2.4 Anomalous $W\gamma$ Production . . . . .	37
2.5 A brief history of $W\gamma$ measurements . . . . .	41
<b>3 Experimental Setup</b>	<b>46</b>
3.1 Large Hadron Collider . . . . .	47
3.2 Compact Muon Solenoid . . . . .	53
3.2.1 Introduction . . . . .	53

3.2.2	Magnet . . . . .	55
3.2.3	Tracking System . . . . .	56
3.2.4	Electromagnetic Calorimeter . . . . .	57
3.2.5	Hadron Calorimeter . . . . .	58
3.2.6	Muon System . . . . .	59
3.2.7	Triggering and Data Aquisition . . . . .	61
3.2.8	Particle Flow Algorithm of Event Reconstruction . . . . .	63
<b>4</b>	<b>CMS Tracker Alignment</b>	<b>65</b>
4.1	Approach . . . . .	66
4.2	Selected Results on Alignment of the Tracking System with 2015 Data	70
4.2.1	Geometry Comparison . . . . .	71
4.2.2	Distributions of Medians of Unbiased Track-Hit Residuals . .	72
4.2.3	Cosmic Track Splitting Validation . . . . .	74
4.2.4	Primary Vertex Validation . . . . .	76
<b>5</b>	<b><math>W\gamma</math> Cross Section Measurement</b>	<b>78</b>
	<b>Bibliography</b>	<b>79</b>

# Chapter 1

## Introduction

Elementary particle physics describes fundamental particles and their interactions. Fundamental particles are the smallest constituents of our Universe. When examined at smaller scales, the substances around us consist of molecules, molecules consist of atoms. In an atom there is a nucleus made of neutrons and protons and some number of electrons occupying orbits around the nucleus. Protons and neutrons have a structure while an electron is not known to have any internal structure, therefore, an electron is an example of a particle which is considered to be fundamental.

Interactions of elementary particles are described by quantum field theories which incorporate principles of the quantum mechanics and the special theory of relativity. The set of such theories, including quantum electrodynamics (QED), quantum chromodynamics (QCD) and the theory of weak interactions is called the Standard Model (SM). Current observations have proved the SM to be an accurate description of elementary particle interactions.

However, there are several experimental observations that are not described by the SM such as effects of gravity, dark matter, dark energy, matter/antimatter

asymmetry and others. Therefore, the SM is not a complete theory of particle interactions. There are several SM extensions offered by theorists as well as radically new theories waiting for experimental confirmation or exclusion.

Some SM extensions and new theories predict the existence of heavy particles with masses lying beyond experimentally reachable energies. The search of these particles is a priority in particle physics. One source of highly energetic elementary particles is cosmic rays. The most energetic particles ever observed came from this source. However, cosmic rays are totally uncontrollable and such highly energetic particles are rare. If we want to produce a large number of particles in a given energy range, we need to use a particle accelerator. A large amount of data allows experimentalists to perform a statistical analysis and increase the probability of finding a new particle if it exists.

Symmetric colliding beams is the most effective way to produce as heavy particles as possible given the energies of the colliding particles. Compared to experiments colliding a single beam at a fixed target, in the case of a symmetric collision the total momentum of two colliding particles is zero and, therefore, much larger fraction of energy can transfer to a mass of a new particle. The Large Hadron Collider (LHC) is one such collider with the highest energy in the world. It can produce the most massive particles to probe physics beyond the SM (BSM).

The Compact Muon Solenoid (CMS) is one of two general-purpose detectors at the LHC. It is placed at one of four collision points. CMS has a broad physics program including searches for the BSM physics as well as the precision measurements of the parameters of the SM itself. The measurement of this dissertation is a SM measurement with CMS data collected in 2012 in  $pp$  collisions of LHC with beam energies of 4 TeV. The result can be compared to the SM prediction. Certain BSM theories predict a deviation of the result of this measurement from its SM

value, therefore, with this measurement, in addition to testing the SM, we also search for a new physics.

The rest of this chapter gives general introductory information about the SM while Ch. 2 concentrates on the theory of the SM and BSM  $W\gamma$  production and also discusses previous measurements of this process. Chapter 3 describes LHC and CMS in more details. Chapter 4 explains one specific detail of the CMS operation that is the spacial alignment of the tracking detector of charged particles. Finally, Ch. 5 describes the details of the measurement of this dissertation and reports the results.

## 1.1 Fundamental Particles and Interactions

The SM describes interactions of elementary particles. There are four fundamental interactions: electromagnetic, strong, weak and gravitational. The gravity is not included into the SM but its effect on particles is negligible compared to the other forces which makes it possible to develop a theory of the particle physics and conduct experiments even without having the gravity included into the model.

All fundamental elementary particles in the SM can be split into three categories by their spins. There are fermions which possess spin  $s=1/2$ , there are gauge bosons which are vector particles ( $s=1$ ) and there is the Higgs boson which is a scalar particle ( $s=0$ ).

The fermions are arranged into three generations, each generation consists of a quark with charge  $Q=+2/3$  (up, charm, and top quarks), a quark with  $Q=-1/3$  (down, strange, and bottom quarks), a charged lepton with  $Q=-1$  (electron, muon, and tau-lepton) and a neutrino (electron, muon, and tau neutrinos) which is electrically neutral. Each quark can carry any of three colors: red, blue, or green. Additionally, each fermion has its antiparticle. Therefore, the total number of fundamental fermions is  $(6(\text{leptons}) + 6(\text{quarks}) \cdot 3(\text{colors})) \cdot 2(\text{to include antiparticles}) = 48$ .

Corresponding particles in different generations have the same charges, spins and interaction properties but masses of particles increase with generation. These mass differences lead to different decay properties because a particle A can decay to particles B and C only if their masses relate as  $m_A > m_B + m_C$ . Thus, an electron is a stable particle, a muon decays as  $\mu^- \rightarrow e^- + \bar{\nu}_e + \nu_\mu$ , a tau-lepton, as the heaviest charged lepton, has the largest number of decay channels amongst the charged leptons:  $\tau^- \rightarrow \mu^- + \bar{\nu}_\mu + \nu_\tau$ ,  $\tau^- \rightarrow e^- + \bar{\nu}_e + \nu_\tau$ ,  $\tau^- \rightarrow \nu_\tau + \text{quarks}$ .

In addition to fermions, the SM includes gauge bosons which are interaction mediators. They are called mediators because fermions interact with each other by exchanging them. For example, two charged fermions can interact with each other by exchanging a photon. Such interaction is called electromagnetic interaction and a photon is a mediator for the electromagnetic interaction. Similarly, a gluon is a mediator for strong interactions, and  $W^\pm$  and  $Z^0$  bosons are mediators for weak interactions.  $W^\pm$  and  $Z^0$  bosons are massive while a photon and a gluon are massless particles.

The last SM particle is the Higgs boson. The Higgs boson is a scalar neutral particle which is playing a critical role in the electroweak symmetry breaking. The Higgs mechanism explains how  $W$  and  $Z$  bosons become massive particles.

All the particles are summarized in Fig. 1.1. These and only these fundamental particles and their antiparticles have been discovered by now. However, there are many composite particles which are called hadrons. Hadrons can consist of three quarks (baryons), quark and antiquark (meson), or three antiquarks (antibaryons). Hadrons always possess an integer charge.

Most of the particles are short-lived and decay within microseconds. The only stable particles are protons and antiprotons, electrons and positrons, neutrinos and antineutrinos, photons, and, in some sense, gluons. However, if a particle cannot decay, it does not mean that it would live forever. There are many different kinds of reactions in which particles can disappear. Antiprotons and positrons would immediately annihilate with protons and electrons, photons can be absorbed by charged particles, electrons and protons can scatter to produce neutrons and neutrinos and many other reactions are possible.

In this dissertation, the study of  $pp \rightarrow W\gamma + X \rightarrow l\nu\gamma$  process where  $\ell = e, \mu$  is presented. The  $W\gamma$  production with leptonic  $W$  decays proceeds through one of

the following three processes: the initial state radiation where a photon is emitted from one of the incoming partons, the final state radiation where a photon is radiated off the charged lepton from the  $W$  boson decay, and, finally, the triple gauge coupling (TGC) where a photon is emitted from the  $W$  boson. Many BSM theories predict an enhancement of the TGC production over the SM value and, therefore, the experimental search for such an enhancement is a good test for such theories.

Therefore, the focus of this study is an interaction between a photon and a  $W$  boson however many other SM particles are relevant too. Thus, a charged lepton and a neutrino appear as the final state particles, a quark and an antiquark appear as initial state particles and all fundamental particles except the Higgs boson participate in various background processes. Subsequent chapters describe these particle interactions in more details.

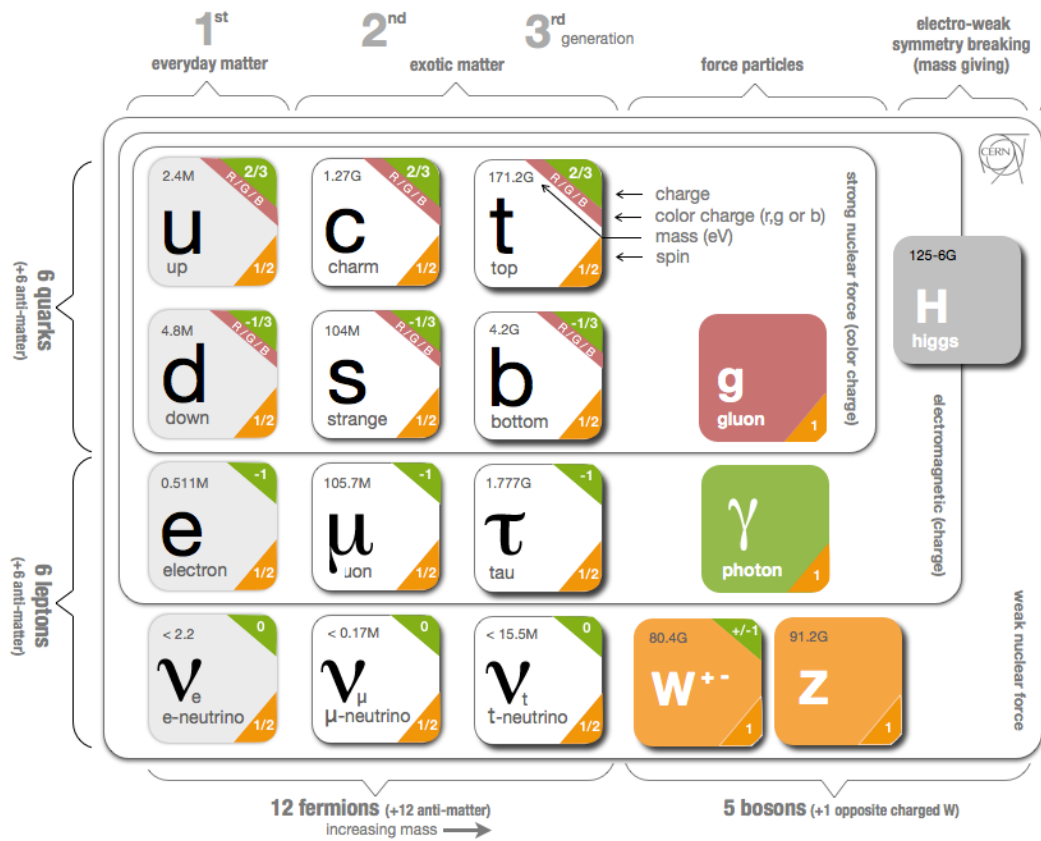


Figure 1.1: Standard Model Particles and Interactions. Source of the figure: [41].

## 1.2 Electroweak Interactions

All electrically charged particles participate in electromagnetic interactions. The theory of electromagnetic interactions is called quantum electrodynamics (QED). All electromagnetic interactions are mediated by a photon, a spin-one electrically neutral massless particle, and can be reduced to one elementary process (Fig. 1.2, left). This process represents a charged fermion radiating or absorbing a photon. Such elementary process itself is forbidden by the energy conservation law but this element is a base of an actual process. For example, the Bhabha scattering,  $e^+e^- \rightarrow e^+e^-$ , occurs through  $e^+e^-$  annihilation with further production of a new  $e^+e^-$  pair (Fig. 1.2, middle) or through exchange of a photon between the positron and the electron (Fig. 1.2, right). Both cases involve nothing except the electromagnetic elementary process (Fig. 1.2, left). Such graphical representations of the particle physics processes are called Feynman diagrams.

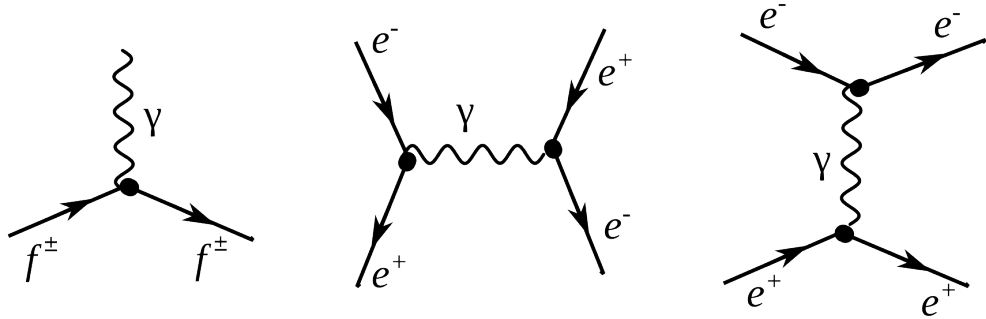


Figure 1.2: Electromagnetic interactions. Left: a photon radiation off a charged fermion, middle and right: Bhabha scattering.

As for the weak interactions, there are two kinds of them: neutral (mediated by a Z boson) and charged (mediated by a  $W^\pm$  boson). Elementary processes with W and Z bosons are shown in Fig. 1.3. Because the electric charge must be conserved

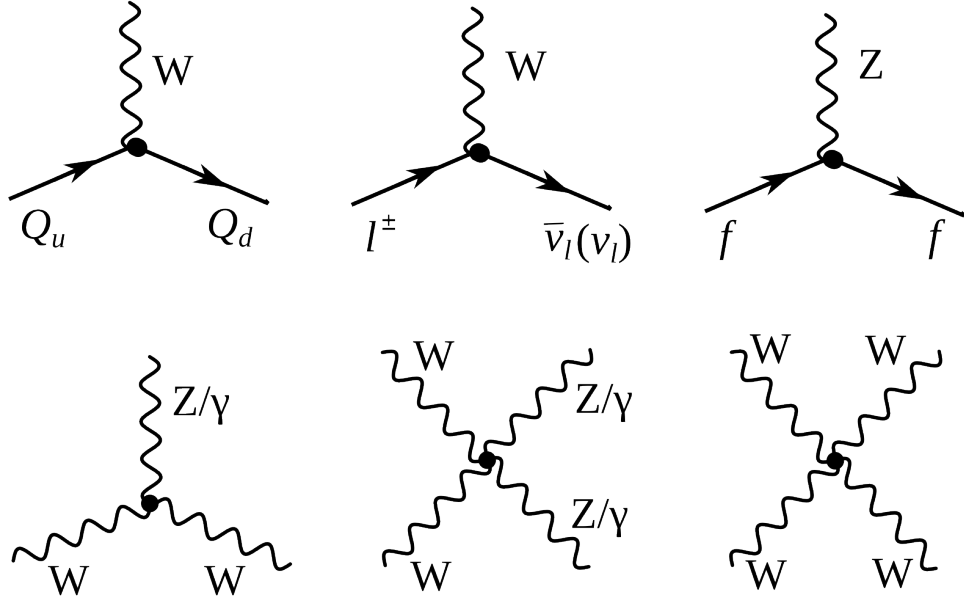


Figure 1.3: Weak elementary processes and gauge couplings. Top left: a quark with charge  $Q=+2/3$  enters, emits a  $W$  boson, and a quark with charge  $Q=-1/3$  escapes. Top middle: a charged lepton enters, emits a  $W$  boson, and a neutrino or antineutrino escapes conserving a lepton flavor number. Top right: a fermion enters, emits a  $Z$  boson and escapes. Bottom left: TGC couplings  $WW\gamma$  and  $WWZ$ . Bottom middle: QGC couplings  $WW\gamma\gamma$ ,  $WWZ\gamma$  and  $WWZZ$ . Bottom right: QGC coupling  $WWWW$ .

at any vertex, a particle radiating or absorbing a  $W$  boson converts to a different particle. Thus, a charged lepton converts to a neutrino (or vice versa) as shown in Fig. 1.3, top middle. Each lepton carries a lepton flavor number (Tab. 1.1). Lepton flavor is conserved in any interaction, thus an electron radiating a  $W$  boson always converts to an electron neutrino, a muon converts to a muon neutrino etc.

From top left diagram in Fig. 1.3 we see that if a quark with  $Q=+2/3$  enters, then a quark with  $Q=-1/3$  escapes and, therefore, the flavor of the quark is changed. The charged weak interaction is the only interaction which changes a quark flavor. The probability of each of three quarks with  $Q=-1/3$  to be born

Table 1.1: Lepton Flavor Number

particles	$L_e$	$L_\mu$	$L_\tau$
$e^-, \nu_e$	+1	0	0
$e^+, \bar{\nu}_e$	-1	0	0
$\mu^-, \nu_\mu$	0	+1	0
$\mu^+, \bar{\nu}_\mu$	0	-1	0
$\tau^-, \nu_\tau$	0	0	+1
$\tau^+, \bar{\nu}_\tau$	0	0	-1

is determined by the Cabibbo-Kobayashi-Maskawa matrix which relates mass eigenstates  $d, c$  and  $b$  to weak eigenstates  $d', c'$  and  $b'$  (Eq. 1.1). Absolute values of the matrix elements are all known (Eq. 1.2) and are the highest for the quark of the same generation as the initial state quark. In the particular case shown in the top left diagram in Fig. 1.3,  $u$  is the initial state quark and  $d$  has the highest probability to be produced after an interaction with a  $W$  boson but  $s$  and  $b$  can also be produced if there is enough energy.

$$\begin{pmatrix} d' \\ s' \\ b' \end{pmatrix} = \begin{pmatrix} V_{ud} & V_{us} & V_{ub} \\ V_{cd} & V_{cs} & V_{cb} \\ V_{td} & V_{ts} & V_{tb} \end{pmatrix} \begin{pmatrix} d \\ s \\ b \end{pmatrix} \quad (1.1)$$

$$\begin{pmatrix} |V_{ud}| & |V_{us}| & |V_{ub}| \\ |V_{cd}| & |V_{cs}| & |V_{cb}| \\ |V_{td}| & |V_{ts}| & |V_{tb}| \end{pmatrix} = \begin{pmatrix} 0.97 & 0.23 & 0.00 \\ 0.23 & 0.97 & 0.04 \\ 0.01 & 0.04 & 1.00 \end{pmatrix} \quad (1.2)$$

An elementary process of a neutral weak interaction is an emission a  $Z$  boson off a fermion line (right top diagram in Fig. 1.3). Diagrams with a  $Z$  boson are very similar to ones with a photon except a photon can only be radiated off a charged particle but a  $Z$  boson can also be radiated off a neutrino or antineutrino.

The bottom diagrams in Fig. 1.3 are gauge bosons coupling diagrams including self-coupling of a  $W$  boson, its interaction with a  $Z$  boson and its electromagnetic radiation of a photon. Charge-conserving TGC and quartic gauge couplings (QGC) containing two or four  $W$  bosons are all possible in the SM:  $WWZ$ ,  $WW\gamma$ ,  $WWZZ$ ,  $WWZ\gamma$ ,  $WW\gamma\gamma$ , and  $WWWW$ .

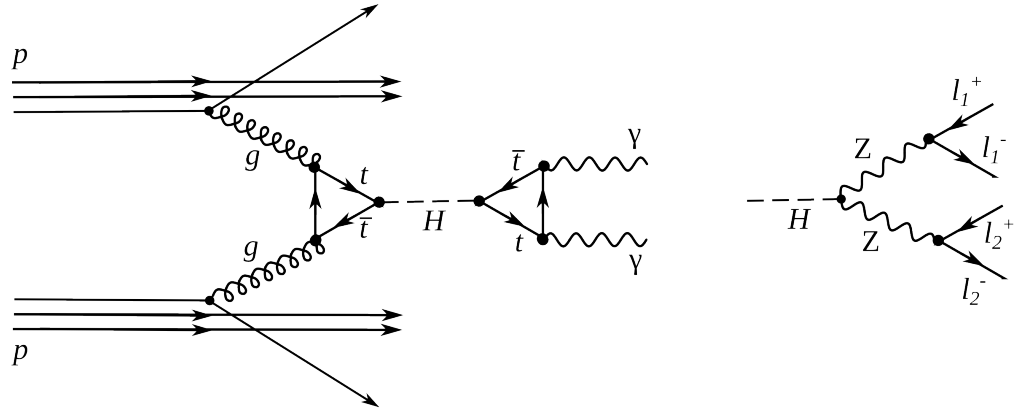


Figure 1.4: The Higgs boson production and decay. Left:  $H \rightarrow \gamma\gamma$ , right:  $H \rightarrow ZZ \rightarrow 4l$ .

Electromagnetic and weak interactions are unified by the electroweak Glashow-Weinberg-Salam (GWS) theory which is based on  $SU(2) \times U(1)$  symmetry.  $SU(2)$  is the symmetry of weak isospin which generates three bosons:  $W^1$ ,  $W^2$  and  $W^3$ .  $U(1)$  is the symmetry of the weak hypercharge and generate one neutral boson  $B$ .  $W^1$  and  $W^2$  are mixed to create  $W^+$  and  $W^-$  mediators while  $W^3$  and  $B$  are mixed to create a  $Z$  boson and a photon. Therefore, the GWS theory considers electromagnetic and weak forces as different manifestations of the electroweak force. The electroweak theory is discussed in greater details in Ch. 2.

Weak interactions are mediated by heavy bosons ( $M_W = 80$  GeV,  $M_Z = 91$  GeV) while electromagnetic interactions are mediated by a massless photon, thus, the electroweak symmetry is broken. To explain this phenomenon, the Higgs

mechanism was introduced. The mechanism predicted an existence of an additional boson: the Higgs boson. The Higgs boson was a missing piece of the SM for many years and was finally discovered in 2012 at LHC by ATLAS and CMS collaborations through the processes shown in Fig. 1.4 [11], [10].

The measurement in this dissertation is an electroweak measurement because the process involves a  $W$  boson. It includes an interaction of a  $W$  boson with leptons and quarks as well as the TGC  $WW\gamma$ . Thus, the measurement is a good test of the SM electroweak theory.

### 1.3 Strong Interactions

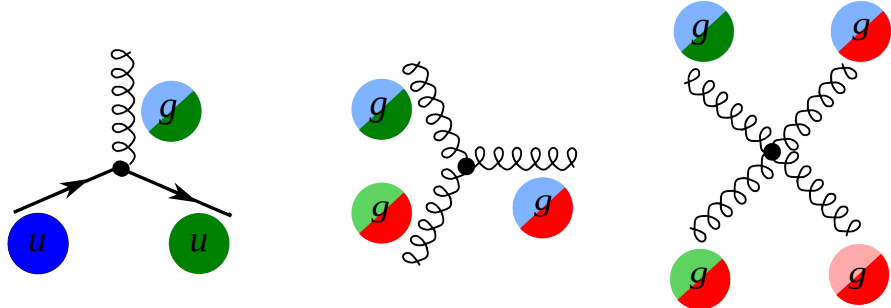


Figure 1.5: Elementary processes of strong interactions

The third fundamental force after the electromagnetic and weak ones is the strong force. The strong force is responsible for gluing protons and neutrons together in the nuclei as well as for forming protons and neutrons themselves. The strong interactions occur by exchanging gluons which are spin-one massless electrically neutral particles.

The elementary strong processes are shown in Fig. 1.5. There are three elementary processes:  $qqg$ ,  $ggg$  and  $gggg$ , all are involving particles with color charges. Thus, gluons couple to quarks and self-couple. Color charges must be conserved at each elementary process of the strong interaction. Each quark possesses one of three colors at a time, and there are eight types of gluons to cover all possible color exchanges.

The coupling constant of the strong interaction depends on the distance between interacting particles: it becomes larger as the distance becomes larger and smaller as the distance becomes smaller. As the distance approaches zero, the coupling constant approaches zero too, and, thus, in the asymptotic limit two quarks located at the same place do not interact. This property is called asymptotic freedom.

On the other hand, when the distance between quarks becomes larger, the coupling constant also becomes larger. This property confines quarks to always stay in the color neutral combinations (hadrons), it forbids the existence of free quarks. A combination becomes color neutral when there is the same amount of color and anticolor or if there is the same amount of each of the three colors. Thus, mesons are comprised of a quark and an antiquark with the opposite color charges, and baryons are composed of three quarks: red, green and blue one. Examples of baryons include such well-known particles as a proton and a neutron.

The asymptotic freedom and the confinement are properties that are specific to strong interactions. The theory of strong interactions is called the quantum chromodynamics (QCD) which is a quantum field theory invariant under  $SU(3)$  color transformations. When the coupling constant is much less than one  $\alpha_s \ll 1$ , the perturbative approach can be used to compute observables.

The  $W\gamma$  process being measured in this dissertation is not intended to test QCD, but a good understanding of QCD is essential for performing this measurement because the QCD corrections to the Feynman diagrams of the process are large and have to be taken into account when producing simulation. In addition, QCD describes the dynamics of quarks and gluons within colliding protons and predicts probabilities of one or another quark-antiquark pair to interact. Physics of proton-proton collisions is discussed in Ch. 1.4.

## 1.4 Physics of Proton-Proton Collisions

Consider a  $pp$  collision at LHC. The proton energies are so high that each proton behaves as a complex structure. A proton is a baryon, it consists of three quarks:  $uud$ . These three quarks are called valence quarks. They interact with each other by exchanging gluons which produce virtual  $q\bar{q}$  pairs (Fig. 1.6). Such virtual quarks are also called sea quarks.

Any parton, quark, antiquark or gluon, from one proton can interact with any parton from another proton. Probabilities  $f_i(x, Q^2)$  of any particular constituent  $i$  to interact are described partially by QCD and partially by experimental measurements and depend on the momentum transfer  $Q$  and the momentum fraction of a specific parton  $x$ . These probabilities are called parton distribution functions (PDFs).

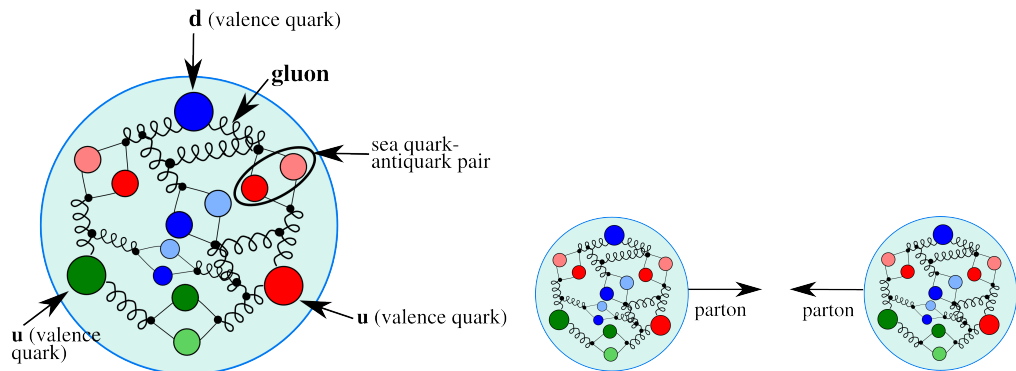


Figure 1.6: The proton structure (left) and the proton-proton collision (right).

For large  $Q^2$  and  $x$  gluon-gluon interactions have the largest probabilities to occur (Fig. 1.7). However, gluons do not couple directly to a  $W$  boson, thus, in the  $W\gamma$  measurement we are mostly interested in quark-antiquark pairs which would have a total charge corresponding to the charge of a  $W$  boson ( $\pm 1$ ). Since

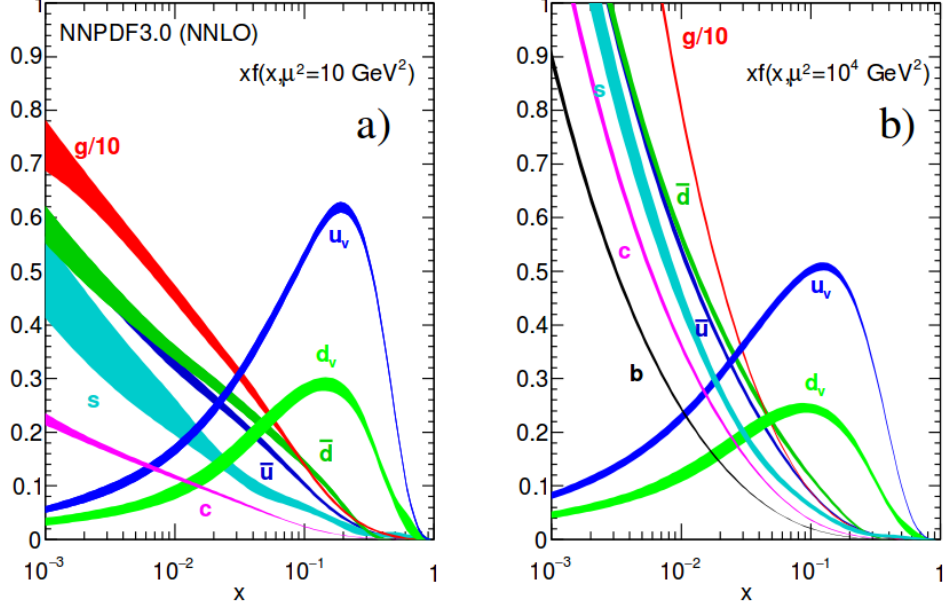


Figure 1.7: Parton distribution functions [31].

we have  $u$  and  $d$  as valence quarks and we know that the probability to couple to the same generation quark in charged weak interactions is the highest, most of the  $W$  bosons are created by  $u\bar{d}$  and  $d\bar{u}$  pairs however other  $q\bar{q}'$  combinations with the total charges of  $\pm 1$  are also possible. As we look for events containing  $W\gamma$  we also have other events mimicking our process. Such background events can be produced by any pair of partons.

## 1.5 Open Questions of the Standard Model

While the SM is an accurate description of all particle physics experimental results, there are certain phenomena which are not included into the SM. In this subsection we discuss some of them.

The gravitational interactions do not fit into the SM. It is the open question whether the quantum theory of gravity is possible and whether there is a mediator of the gravitational interactions. Also, it is not known why the gravitational force is so much weaker than the other forces. One possible explanation comes from a theory which predicts extra spatial dimensions beyond the three we experience (e.g. the string theory). In this case, it is possible that the gravitational force is shared with other dimensions and only a fraction is available in our three dimensions.

Another mystery of the universe is its composition: it is known from the studies of the gravitational effects that our universe consists of dark energy by 68%, of dark matter by 27% and of baryon matter only by 5% [30]. The dark energy resists the gravitational attraction and accelerates the expansion of the universe, and is not detectable by any effects except gravitational. The understanding of dark energy is a question of general relativity rather than particle physics. The dark matter, however, likely consists of particles and therefore is a subject of particle physics. It does not radiate and that is why it cannot be detected by telescopes. The nature of the dark matter is not known but its constituents must be very stable to remain since the Big Bang. The theory of the supersymmetry which is unifying fundamental particles and mediators predicts many of new heavy particles and the lightest supersymmetric particle, the neutralino, is a good candidate for dark matter.

One more open question is the reason for the matter/antimatter asymmetry.

Matter and antimatter should have been created in the same amount at the moment of the Big Bang. Most of it has annihilated but because of asymmetry, there was more matter than antimatter which led to the state of the Universe we observe now. There is a phenomenon of the CP-violation in weak interactions observed and described which predicts the asymmetry at a certain level. However, the effect of the CP-violation is not large enough to account for the observed amount of the matter and, therefore, the total matter/antimatter asymmetry remains unexplained.

The measurement of the photon transverse momentum spectrum ( $P_T^\gamma$ ) of the  $W\gamma$  process has a goal to both test the SM and search for the BSM physics. The low  $P_T^\gamma$  region is not expected to be affected by any new physics and must agree well with the SM predictions while the high  $P_T^\gamma$  region may indicate an existence of new physics if there is an enhancement over the SM predictions. The excess would be indirect evidence of the BSM particles like supersymmetric particles or additional gauge bosons which could be part of the explanation of the dark matter presence or difference in magnitudes of different interactions. More theoretical details about the SM description of  $W\gamma$  process as well as possible BSM physics are given in Ch. 2.

## Chapter 2

# **$W\gamma$ Production Theory and Former Experimental Results**

Chapter 2 provides deeper theoretical background for the measurement of this dissertation and discusses former experimental results. The derivation of the electroweak Lagrangian is described in Ch. 2.1, including the appearance of triple gauge coupling (TGC) and quartic gauge coupling (QGC) terms. Then concepts of the cross section and the luminosity are discussed in Ch. 2.2. More specific details regarding the SM cross section of  $W\gamma$  are summarized in Ch. 2.3. Possible causes and potential effects of anomalous TGC (aTGC) are explained in Ch. 2.4. Finally, Ch. 2.5 lists former physics experiments which probed the same aTGC vertex which is probed in the measurement of this dissertation including measurements of exactly the same process at lower LHC beam energy.

## 2.1 Electroweak Theory of the Standard Model

To develop a quantum field theory, we start with the Lagrangian of free fermions. In order to describe a system with a conserved physical quantity, the Lagrangian is required to satisfy a local invariance with respect to a certain transformation. For instance, a conservation of electric charge requires local invariance under  $U(1)$  transformation for the QED Lagrangian [34]. The requirement of local invariance introduces an interaction between one or more new vector fields and our free fermions. The new vector fields are mediators of an interaction conserving the physical quantity. To provide a full description for a new boson field, in addition to the interaction term we introduce an invariant term for the kinetic energy of the boson. Such an approach allows us to derive a Lagrangian which is locally invariant with respect to a certain gauge transformation and contains interacting fermions as well as interaction mediators.

The SM is a quantum field theory invariant under the local  $SU(3)_C \times SU(2)_L \times U(1)_Y$  transformation [34]. The SM Lagrangian includes all observed quantum fields and their interactions.

The part of the SM Lagrangian based on the  $SU(3)_C$  symmetry is called QCD or the theory of strong interactions. QCD has three types of charges which are called colors: red, blue, and green. To be a subject of the strong interaction, a fermion must possess a color charge. Quarks and antiquarks are such fermions. The requirement to satisfy the gauge invariance with respect to  $SU(3)_C$  transformations generates eight massless gluons, and the non-abelian nature of the  $SU(3)$  group generates self-interactions of gluons including three-gluon and four-gluon vertices.

The part of the SM Lagrangian based on the  $SU(2)_L \times U(1)_Y$  symmetry is the foundation of the unified theory of electroweak interactions.  $SU(2)_L$  reflects

transformations in the weak isospin space of left-handed fermions ([18], Ch. 9) while  $U(1)_Y$  reflects transformations in a weak hypercharge space of all fermions. The requirement of the local gauge invariance generates four massless vector bosons which are mediators of electromagnetic and weak interactions. The non-abelian structure of the  $SU(2)$  group generates gauge boson self-couplings the same way as self-interactions of gluons appear in QCD.

Mass terms for the vector bosons would violate the gauge invariance of the electroweak Lagrangian, however it is experimentally known that the mediators of weak interactions are heavy particles with masses  $M_W = 80$  GeV and  $M_Z = 91$  GeV. A possible solution of this discrepancy is the mechanism of Spontaneous Symmetry Breaking.

The mechanism of Spontaneous Symmetry Breaking and the appearance of the mass terms for  $W$  and  $Z$  bosons is realized by introducing an additional doublet of scalar fields. After that, the Lagrangian is transformed in such a way that  $W$  and  $Z$  bosons acquire masses through their interactions with a new particle: the Higgs boson ( $H$ ). A photon does not couple to the Higgs boson remaining a massless particle and leaving QED symmetry group  $U(1)$  to be unbroken.

The measurement in this dissertation provides a test for the electroweak sector of the SM. We will retrace the steps of the derivation of the electroweak part of the SM Lagrangian starting from the terms for free fermions. The resulting Lagrangian accommodates electroweak gauge bosons and their self-couplings. One of these self-couplings,  $WW\gamma$ , is the primary focus of our measurement.

It is experimentally known that the dynamics of weak interactions depend on particle chirality ([18], chapter 4.4.1). In particular, a  $W$  boson couples to left-handed fermions and right-handed antifermions only. Given different properties of left-handed and right-handed fermions, they are treated differently by the

electroweak theory.  $SU(2)$  doublets are introduced for the wave functions of left-handed fermions while  $SU(2)$  singlets are introduced for the wave functions of right-handed fermions. Equations 2.1 and 2.2 show wave functions for the first generation fermions. Wave functions for the other two generations are constructed the same way.

$$\psi_1(x) = \begin{pmatrix} u \\ d' \end{pmatrix}_L, \psi_2(x) = u_R, \psi_3(x) = d'_R. \quad (2.1)$$

$$\psi_1(x) = \begin{pmatrix} \nu_e \\ e^- \end{pmatrix}_L, \psi_2(x) = \nu_{eR}, \psi_3(x) = e^-_R. \quad (2.2)$$

The state  $d'$  in Eq. 2.1 is a weak eigenstate which is a linear combination of the mass eigenstates of the  $d$ ,  $c$  and  $b$  quark wave functions and is determined by the quark mixing matrix,  $V$ , which is also called Cabibbo-Kobayashi-Maskawa matrix [34]:

$$\begin{pmatrix} d' \\ c' \\ b' \end{pmatrix} = V \begin{pmatrix} d \\ c \\ b \end{pmatrix} \quad (2.3)$$

To derive the unified electroweak Lagrangian, we start with the free fermion terms:

$$L_0 = \sum_{j=1}^3 i\bar{\psi}_j(x)\gamma^\mu\partial_\mu\psi_j(x), \quad (2.4)$$

where  $\gamma^\mu$  are Dirac matrices ([18], chapter 7.1) and  $\psi_j(x)$  are wave functions determined by Eqs. 2.1 and 2.2.

The wave function  $\psi_1$  changes under the  $SU(2)_L \times U(1)_Y$  transformations in

the following way:

$$\psi_1(x) \rightarrow e^{iy_1\beta} U_L \psi_1(x), \quad (2.5)$$

while the wave functions  $\psi_{(2,3)}(x)$  are singlets of  $SU(2)_L$  and are affected only by  $U(1)$  transformations:

$$\psi_{(2,3)}(x) \rightarrow e^{iy_{(2,3)}\beta} \psi_{(2,3)}(x). \quad (2.6)$$

The transformation in the weak isospin space is defined as  $U_L \equiv e^{i\sigma_i \alpha_i / 2}$  where  $\sigma_i$  are Pauli matrices ([18], chapter 4.2.2). Phases  $\alpha_i(x)$  and  $\beta(x)$  in Eqs. 2.5 and 2.6 are arbitrary functions of  $x$ , and  $y_{(1,2,3)}$  are weak hypercharges which are named analogous to electric charges in QED.

In order for the Lagrangian to satisfy the local  $SU(2)_L \times U(1)_Y$  invariance, partial derivatives in Eq. 2.4 have to be substituted with covariant derivatives:

$$D_\mu \psi_1(x) = [\partial_\mu - ig\tilde{W}_\mu(x) - ig'y_1 B_\mu(x)] \psi_1(x) \quad (2.7)$$

$$D_\mu \psi_{(2,3)}(x) = [\partial_\mu - ig'y_{(2,3)} B_\mu(x)] \psi_{(2,3)}(x) \quad (2.8)$$

where  $g, g'$  are arbitrary constants,

$$\tilde{W}_\mu(x) \equiv \frac{\sigma_i}{2} W_\mu^i(x) = \frac{1}{\sqrt{2}} \begin{pmatrix} \sqrt{2}W_\mu^3 & (W_\mu^1 - iW_\mu^2)/\sqrt{2} \\ (W_\mu^1 + iW_\mu^2)/\sqrt{2} & -W_\mu^3 \end{pmatrix}, \quad (2.9)$$

$B_\mu, W_\mu^1, W_\mu^2, W_\mu^3$  are four vector bosons that arise from the requirement that the Lagrangian is invariant under local  $SU(2)_L \times U(1)$  transformations.

The Lagrangian becomes:

$$L_0 \rightarrow L = \sum_{j=1}^3 i\bar{\psi}_j(x)\gamma^\mu D_\mu \psi_j(x) \quad (2.10)$$

To make new vector bosons physical fields it is necessary to add terms for their kinetic energies:

$$L_{KIN} = -\frac{1}{4}B_{\mu\nu}B^{\mu\nu} - \frac{1}{4}W_{\mu\nu}^i W_i^{\mu\nu} \quad (2.11)$$

where  $B_{\mu\nu} \equiv \partial_\mu B_\nu - \partial_\nu B_\mu$ ,  $W_{\mu\nu}^i \equiv \partial_\mu W_\nu^i - \partial_\nu W_\mu^i + g\epsilon^{ijk}W_\mu^j W_\nu^k$

Off-diagonal terms of  $\tilde{W}_\mu$  are wave functions of charged vector bosons

$$W^\pm = (W_\mu^1 \mp iW_\mu^2)/\sqrt{2} \quad (2.12)$$

while  $W_\mu^3$  and  $B_\mu$  are neutral fields which are mixtures of a  $Z$  boson and a photon determined by:

$$\begin{pmatrix} W_\mu^3 \\ B_\mu \end{pmatrix} \equiv \begin{pmatrix} \cos\theta_W & \sin\theta_W \\ -\sin\theta_W & \cos\theta_W \end{pmatrix} \begin{pmatrix} Z_\mu \\ A_\mu \end{pmatrix} \quad (2.13)$$

where  $\theta_W$  is the electroweak mixing angle and  $A_\mu$  is a photon field.

In order to be consistent with QED, terms involving  $A_\mu$  in the electroweak Lagrangian must be equal to the corresponding terms in the QED Lagrangian [34]:

$$L_{QED} = i\bar{\psi}(x)\gamma^\mu \partial_\mu \psi(x) - m\bar{\psi}(x)\psi(x) + qA_\mu(x)\bar{\psi}(x)\gamma^\mu \psi(x) - \frac{1}{4}F_{\mu\nu}(x)F^{\mu\nu}(x), \quad (2.14)$$

where  $q$  is electric charge of  $\psi(x)$  field,  $F_{\mu\nu} \equiv \partial_\mu A_\nu - \partial_\nu A_\mu$ .

This requirement relates  $g$ ,  $g'$ ,  $\theta_W$  and  $e$  as  $g \sin \theta_W = g' \cos \theta_W = e$  and provides an expression for weak hypercharges:  $y = q - t_3$ , where  $q$  is the electric charge and  $t_3$  is the  $z$ -component of the weak isospin. This results in  $y_1 = 1/6$ ,  $y_2 = 2/3$ , and  $y_3 = -1/3$  for quarks and  $y_1 = -1/2$ ,  $y_2 = 0$ , and  $y_3 = -1$  for leptons. A right-handed neutrino has a weak hypercharge of  $y_2 = 0$ . It also does not have an electric charge, and as a right-handed fermion has  $t_3 = 0$ , therefore, it does not couple to a  $W$  boson. Thus, a right-handed neutrino does not participate in any SM interaction.

Writing  $\tilde{W}_\mu$  in Eq. 2.11 explicitly, we obtain triple gauge coupling (TGC) and quartic gauge coupling (QGC) terms:

$$L_{TGC} = -\frac{g}{4}(\partial_\mu W_\nu^i - \partial_\nu W_\mu^i)\epsilon^{ijk}W^{\mu j}W^{\nu k} - \frac{g}{4}\epsilon^{ijk}W_\mu^jW_\nu^k(\partial^\mu W^{\nu i} - \partial^\nu W^{\mu i}) \quad (2.15)$$

$$L_{QGC} = -\frac{g^2}{4}\epsilon^{ijk}\epsilon^{ilm}W_\mu^jW_\nu^kW_\lambda^{\mu l}W^{\nu m} \quad (2.16)$$

Substituting expressions for  $W_\mu^i$  and  $B_\mu$  determined by Eqs. 2.12 and 2.13 into Eqs. 2.15 and 2.16 we receive charged TGC and QGC terms in the Lagrangian (those involving two or four  $W$  bosons) in the forms of Eqs. 2.17 and 2.20, but all neutral TGC and QGC terms (those not involving any  $W$  bosons) cancel out.

Equation 2.17 involves  $WWZ$  (Eq. 2.18) and  $WW\gamma$  (Eq. 2.19) interactions:

$$L_{TGC} = L_{TGC}^{(1)} + L_{TGC}^{(2)}, \quad (2.17)$$

$$L_{TGC}^{(1)} = -ie \cot \theta_W (W^{-\mu\nu} W_\mu^+ Z_\nu - W^{+\mu\nu} W_\mu^- Z_\nu + W_\mu^- W_\nu^+ Z^{\mu\nu}), \quad (2.18)$$

$$L_{TGC}^{(2)} = -ie (W^{-\mu\nu} W_\mu^+ A_\nu - W^{+\mu\nu} W_\mu^- A_\nu + W_\mu^- W_\nu^+ A^{\mu\nu}). \quad (2.19)$$

Equation 2.20 involves  $WWWW$  (Eq. 2.21),  $WWZZ$  (Eq. 2.22),  $WWZ\gamma$  (Eq. 2.23), and  $WW\gamma\gamma$  (Eq. 2.24) interactions:

$$L_{QGC} = L_{QGC}^{(1)} + L_{QGC}^{(2)} + L_{QGC}^{(3)} + L_{QGC}^{(4)}, \quad (2.20)$$

$$L_{QGC}^{(1)} = -\frac{e^2}{2 \sin^2 \theta_W} (W_\mu^+ W^{-\mu} W_\nu^+ W^{-\nu} - W_\mu^+ W^{\mu} W_\nu^- W^{-\nu}), \quad (2.21)$$

$$L_{QGC}^{(2)} = -e^2 \cot^2 \theta_W (W_\mu^+ W^{-\mu} Z_\nu Z^\nu - W_\mu^+ Z^\mu W_\nu^- Z^\nu), \quad (2.22)$$

$$L_{QGC}^{(3)} = -e^2 \cot \theta_W (2W_\mu^+ W^{-\mu} Z_\nu A^\nu - W_\mu^+ Z^\mu W_\nu^- A^\nu - W_\mu^+ A^\mu W_\nu^- Z^\nu), \quad (2.23)$$

$$L_{QGC}^{(4)} = -e^2 (W_\mu^+ W^{-\mu} A_\nu A^\nu - W_\mu^+ A^\mu W_\nu^- A^\nu). \quad (2.24)$$

In the measurement of this dissertation we probe  $WW\gamma$  coupling (Eq. 2.19).

The unified electroweak Lagrangian discussed above involves kinetic energy terms for fermions and gauge bosons as well as interactions of fermions with gauge bosons, TGC, and QGC. However, this Lagrangian does not contain any

mass terms. Because left-handed and right-handed wave functions transform differently under the electroweak symmetry, adding fermion mass terms of  $\frac{1}{2}m_f^2\bar{\psi}\psi$  would violate the Lagrangian invariance and, therefore, fermion mass terms are forbidden by the  $SU(2) \times U(1)$  symmetry requirement. Mass terms for gauge bosons also would violate the Lagrangian invariance just as a photon mass term  $\frac{1}{2}m^2A^\mu A_\mu$  would violate  $U(1)$  invariance of  $L_{QED}$  [18]. Therefore, Lagrangian  $L$  in Eq. 2.10 contains massless particles only.

However, it is known from experiments that the  $Z$  and  $W$  bosons as well as fermions are massive particles and, therefore, our theory should accommodate their masses. To introduce masses into the electroweak Lagrangian, an  $SU(2)_L$  doublet of complex scalar fields  $\phi(x)$  is added to the Lagrangian:

$$\phi(x) \equiv \begin{pmatrix} \phi^{(+)}(x) \\ \phi^{(0)}(x) \end{pmatrix} \quad (2.25)$$

By selecting a special gauge of  $\phi(x)$  it is possible to spontaneously break electroweak symmetry, generate a new scalar particle, the Higgs boson [34], and introduce mass terms for  $W$  and  $Z$  bosons and charged fermions through their couplings to the Higgs boson. The strength of the coupling constant is proportional to the square of the particle's mass, therefore, heavier particles are more likely to interact with  $H$ , and massless particles do not couple to  $H$ .

The mechanism of generating a fermion's mass involves both left-handed and right-handed components of the fermion. If our hypothesis that right-handed neutrinos do not exist is right, then the Higgs mechanism does not generate neutrino masses. However, from the experiments of neutrino oscillations, neutrinos are known to have masses even though they are orders of magnitude smaller than those of other fermions. Several hypotheses have been offered to resolve this

contradiction however at the moment the mechanism for neutrinos to acquire masses remain unknown [31].

In this dissertation, we study an electroweak process  $W\gamma \rightarrow l\nu_l\gamma$  and probe the TGC vertex  $WW\gamma$  (Eq. 2.19). To do that, we measure the differential cross section of  $W\gamma \rightarrow l\nu_l\gamma$  with respect to the photon transverse momentum. The concept of the cross section in particle physics is discussed in the next chapter.

## 2.2 Cross Section and Luminosity

In this dissertation we measure the total cross section of the process  $pp \rightarrow l\nu_l\gamma + X$  and its differential cross section in transverse momentum of the photon. A cross section in particle physics is an interaction probability per unit flux of incident particles [27]. It can be interpreted as an area which must be crossed by an incident particle in order to interact with a scattering center, or, in case of a differential cross section, area  $d\sigma$  within which an incident particle must appear to be scattered off by an angle  $d\theta$  (Fig. 2.1). The relationship between  $d\sigma$  and  $d\theta$  gives us the expression for a differential cross section  $d\sigma/d\theta$ . Integrating over  $d\theta$ , we obtain the total cross section  $\sigma$ . The cross section concept illustrated in Fig. 2.1 is generalized to be an effective area, and is generalized for two (or more) particle interactions rather than a light particle scattering off a stationary center.

The angle  $\theta$  here is used only as an illustration of a concept of differential cross section. In particle physics we measure a differential cross section with respect to a parameter  $X$  which can be a parameter of one of final state particles or of a system of final state particles. For example, a cross section could be measured as a function of the transverse momentum of a final state photon  $P_T^\gamma$ , the invariant mass of two final state leptons  $m_{ll}$ , or even discreet observables such as the number of jets associated with the process  $N_{jets}$ .

In the scenario illustrated in Fig. 2.1, the number of particles passing through the area  $\sigma$  per unit time is

$$N = L \cdot \sigma, \quad (2.26)$$

where  $L$  is the flux of incident particles and is called luminosity. For colliding beams, the luminosity is determined by collisions frequency, the number of col-

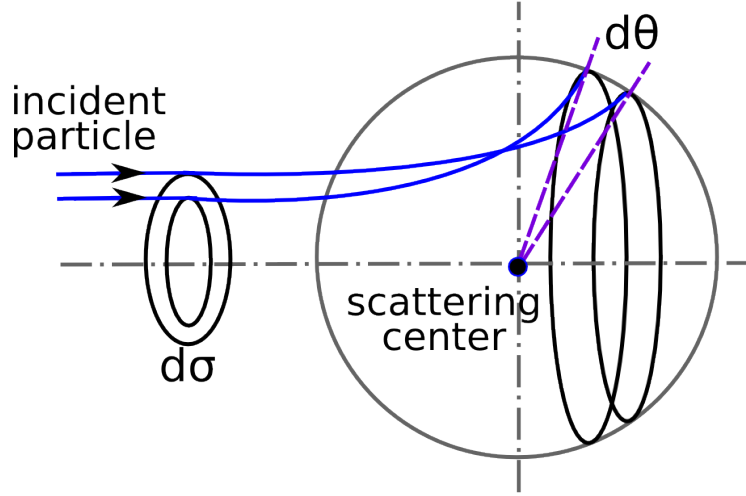


Figure 2.1: Illustration of the differential cross section concept in the classical case.

liding particles in each beam, and beams cross sections. The cross section  $\sigma$  of a specific process can be determined from an experiment as  $\sigma = N/L$ .

A cross section can be computed theoretically using the following expression:

$$\sigma = \frac{W_{fi}}{F} N_{fs}, \quad (2.27)$$

where  $W_{fi}$  is a transition probability between final and initial states of the system per unit spatial volume,  $F$  is the initial flux, and  $N_{fs}$  is the density of final states ([19], chapter 4.3). The initial flux in this expression is determined as number of incident particles per unit volume multiplied by their velocity and by the number of target particles per unit volume.

The formula for the cross section relevant for our measurement, two particles to three final state particles scattering  $1 + 2 \rightarrow 3 + 4 + 5$ , is determined by the Fermi's Golden Rule [18]:

$$\sigma = \frac{1}{4\sqrt{(p_1 p_2)^2 - (m_1 m_2)^2}} \int |M|^2 (2\pi)^4 \delta^4(p_1 + p_2 - p_3 - p_4 - p_5) \prod_{j=3}^5 \frac{1}{2\sqrt{\bar{p}_j^2 + m_j^2}} \frac{d^3 \bar{p}_j}{(2\pi)^3}, \quad (2.28)$$

where  $p_i$  are four-momenta and  $\bar{p}_i$  are three momenta of the initial state and the final state particles,  $m_i$  are masses of particles,  $M$  is the process amplitude determined by the dynamics of the particles interaction. All possible momenta of the final state particles is called the phase space.

During proton-proton collisions at high energy, the hard scattering process occurs between partons in the protons, as discussed in Ch. 1.4. Therefore, the cross section of a process  $pp \rightarrow X + Y$  has two ingredients: PDFs and a partonic cross section  $\sigma_{ab \rightarrow X}$ . The partonic cross section is described by perturbative QCD while PDFs require non-perturbative computations and are determined, in part, from experiments (Fig. 1.7). According to the QCD factorization theorem [20]:

$$\sigma(pp \rightarrow X + Y) = \sum_{a,b} \int dx_a dx_b f_a(x_a, Q^2) f_b(x_b, Q^2) \sigma(ab \rightarrow X). \quad (2.29)$$

In the case of  $W\gamma$  process,  $X$  is  $l\nu\gamma$ ,  $ab$  are  $q_i\bar{q}_j$  or  $q_j\bar{q}_i$ .  $Q^2$  is the large momentum scale that characterizes hard scattering,  $f_a$  and  $f_b$  are PDFs,  $x_a$  and  $x_b$  are fractions of momenta of the partons. In the next sections we will discuss the computation of partonic cross sections of the  $W\gamma$  process and possible BSM effects.

## 2.3 Standard Model $W\gamma$ Production

A  $W$  boson in proton-proton collisions can be produced in the processes  $q\bar{q}' \rightarrow W$  where  $q$  and  $\bar{q}'$  are a quark and an antiquark which have a total charge of  $+1$  if producing a  $W^+$  boson or  $-1$  if producing a  $W^-$  boson. The processes  $u\bar{d} \rightarrow W^+$  and  $d\bar{u} \rightarrow W^-$  are the most likely to occur because  $u$  and  $d$  are valence quarks in a proton. There are twice as many  $u$  quarks in a proton as  $d$  quarks, therefore,  $W^+$  is produced twice more frequently than  $W^-$ . Antiquarks  $\bar{d}$  and  $\bar{u}$  come from the sea  $q\bar{q}$  pairs of the other proton.

Once created, a  $W$  boson decays immediately, its lifetime is  $\simeq 10^{-25}$  s. In an experiment one detects its decay products rather than the  $W$  boson itself. Decay modes of a  $W$  boson include  $W^\pm \rightarrow l^\pm \nu_l (\bar{\nu}_l)$  where  $l^\pm = e^\pm, \mu^\pm$  or  $\tau^\pm$  with branching fractions of 11% per a leptonic channel [31]. The remaining 67% account for various  $W \rightarrow q\bar{q}'$  decays. In this dissertation we only consider  $W^\pm \rightarrow \mu^\pm \nu_\mu (\bar{\nu}_\mu)$  and  $W^\pm \rightarrow e^\pm \nu_e (\bar{\nu}_e)$  channels.

A photon can be emitted from any charged particle of the process: a quark, an antiquark, a charged lepton or a  $W$  boson (Fig. 2.2, top). A quark and an antiquark are initial state particles and, therefore, if one of them radiates a photon, we refer to the process as initial state radiation (ISR). A muon or an electron is a final state particle and if it radiates a photon, we call such a process final state radiation (FSR). Finally, a  $W$  boson is a gauge boson and if it radiates a photon, the process has a vertex with three gauge bosons:  $WW\gamma$ , and we call such process the triple gauge coupling (TGC). We cannot distinguish between these processes experimentally because we detect final state particles only.

The electroweak Lagrangian is described in Chapter 2.1. It is possible to derive equations of motion from the Lagrangian for any fields involved [18]. However, in

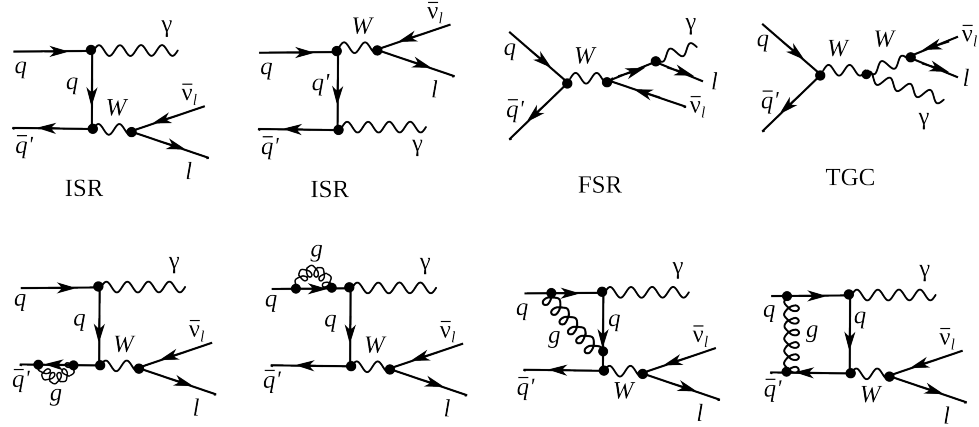


Figure 2.2: Feynman diagrams of  $W\gamma$  production. Top: LO diagrams, bottom: several examples of NLO in QCD.

a quantum field theory equations of motion cannot be solved exactly and, therefore, the perturbative approach is used if a coupling constants is  $g \ll 1$ .

To represent the process graphically Feynman diagrams were invented. Also the diagrams can be used to calculate the process amplitude  $M$  in Eq. 2.28 because they are determined by Lagrangian terms relevant to the process. There are an infinite number of Feynman diagrams corresponding to any specific process and the total amplitude of the process is a sum of individual amplitudes of each diagram and it is not technically possible to take into account all of them. Each vertex introduces a factor in the amplitude of the process that is proportional to the coupling constant. If the coupling constant is  $g \ll 1$ , the perturbative approach arranges all the diagrams by orders of contribution, and, therefore, the Feynman diagrams with fewer vertices would give a significantly larger contribution to the amplitude. In Fig. 2.2 examples of the Leading Order (LO) and the Next-to-Leading Order (NLO) Feynman diagrams are shown (top and bottom diagrams respectively).

At LO, the  $W\gamma$  process is represented by four Feynman diagrams including one FSR, one TGC and two ISR diagrams. Each LO diagram has three vertices. The first calculation of the  $W\gamma$  process with necessary expressions can be found in [43].

The NLO corrections to the amplitude of the  $W\gamma$  process that are shown in Fig. 2.2 are QCD corrections only, which include gluon loops at the same quark line and exchange of a gluon between two different quark lines, however, QED and weak NLO diagrams are also possible. QED corrections involve radiations of extra photons by charged particles, exchange of photons between different charged particles or a photon can be radiated and absorbed by the same charged particle forming a loop. Similarly, weak corrections involve extra virtual  $W$  or  $Z$  bosons. The QCD corrections are the largest among the discussed correction types because the QCD coupling constant is the largest.

A theoretical cross section in particle physics is compared to a measurement result to test the predictions of the model. Also the theoretical cross section is used for producing simulated data. In a simulation, a large set of  $pp$  collisions resulting in a physics process of interest is modeled to create a data set that mimics real data. A typical simulation consists of two parts: the generation of the process and the simulation of particles paths through the detector. The first stage contains a collection of events with final state particles with kinematic quantities distributed according to theoretical predictions for a given process. This stage relies on the theory including the cross section and also all dynamics of the process. The second stage simulates the interaction with media during propagation of particles through the model of the detector as well as the response of detector electronics. In its final form, a simulated dataset has the same format and content of detector signals for each event as real data, and can undergo the same reconstruction and analysis

procedure as real data would.

The most precise theoretical  $W\gamma$  cross section available is the Next-to-Next-to-Leading Order (NNLO) cross section in QCD [45]. The effects of the NNLO correction over the NLO correction and over the LO result are shown in Fig. 2.3 for the transverse mass of the final state particles  $m_T^{l\nu\gamma}$  and for the rapidity difference between a charged lepton and a photon  $\Delta_{l\gamma}$ . The NNLO and NLO theoretical predictions for the photon transverse momentum  $p_T^\gamma$  are overlaid with the 7 TeV ATLAS result. The contribution from higher order corrections is estimated to be  $\pm 4\%$ . However, the NNLO theoretical result was published only recently, in 2015, and no NNLO  $W\gamma$  simulation is available at this time. The simulation used in this analysis is LO + up to two hadronic jets simulation which was found to give the same predictions as the NLO result.

Certain BSM theories predict an enhancement of the contribution from the TGC diagram over the SM prediction. The discussion of these BSM effects and how they affect the  $W\gamma$  process takes place in Ch. 2.4.

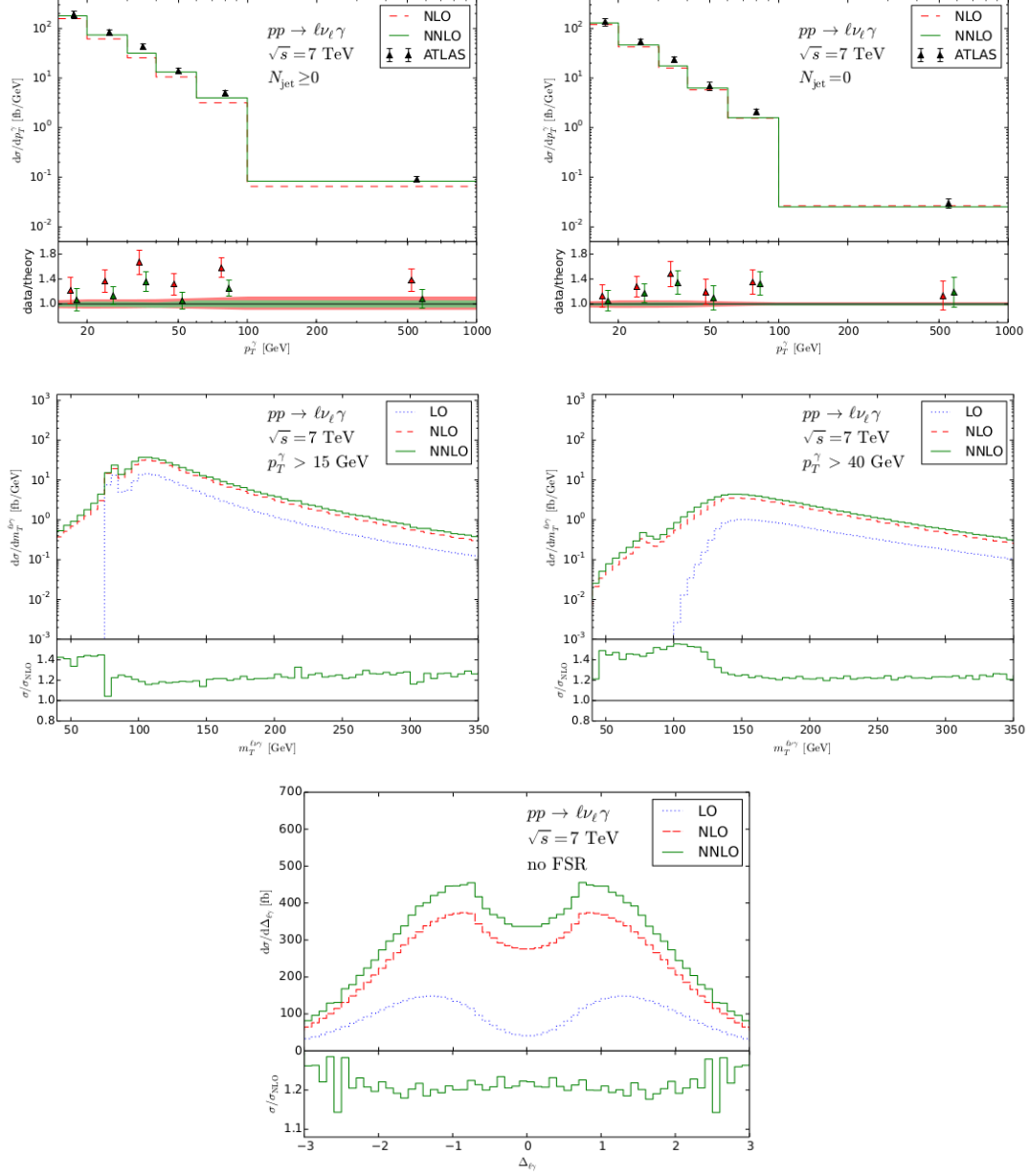


Figure 2.3: Theory spectra. Top: NLO and NNLO  $p_T^\gamma$  spectra of  $W\gamma \rightarrow l\nu\gamma$  at  $\sqrt{s} = 7$  TeV overlaid with ATLAS data for  $N_{jet} \geq 0$  (left) and  $N_{jet} = 0$  (right). Middle: LO, NLO and NNLO  $m_T^{l\nu\gamma}$  spectra of  $W\gamma \rightarrow l\nu\gamma$  at  $\sqrt{s} = 7$  TeV for  $P_T^\gamma > 15$  GeV (left) and  $P_T^\gamma > 40$  GeV (right). Bottom: LO, NLO and NNLO  $\Delta_{l\gamma}$  spectra of  $W\gamma \rightarrow l\nu\gamma$  at  $\sqrt{s} = 7$  TeV.

## 2.4 Anomalous $W\gamma$ Production

Most BSM physics theories predict the existence of particles with masses lying beyond the discovered energy range. If their masses are not accessible even at the accelerators with the highest energies, the direct detection of such particles is not possible. However, loops of heavy particles can affect diagrams of productions of lighter particles. They would give additional contributions to TGC and QGC couplings and, therefore, to the amplitudes to the processes involving TGC and QGC productions. There would be a different number of events produced in the process than one would expect based on SM predictions as shown in Fig. 2.5.

TGC and QGC couplings can be probed by precision measurements of SM processes of diboson and triboson productions because these processes can occur through TGC and QGC. TGC and QGC are represented by vertices with three and four bosons (Fig. 2.4). As discussed in Ch. 2.1, charged TGC and QGC are possible at tree level in the SM while neutral TGC and QGC are not.

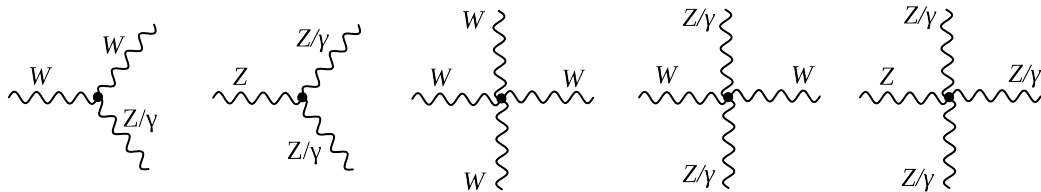


Figure 2.4: Charged TGC (first), neutral TGC (second), charged QGC (third and fourth), and neutral QGC (fifth) vertices.

To account for the effects from the potential loops of heavy particles, we introduce an effective Lagrangian with arbitrary values of coupling constants which can be reduced to the SM Lagrangian if these constants would have their SM values. Introducing the effective Lagrangian makes searches model-independent

because we do not specify particles that form the loops but instead just check whether there is a deviation from the SM prediction in measured observables.

In  $W\gamma$  measurement we can probe  $WW\gamma$  vertex. The most general Lorentz invariant Lagrangian terms of  $WW\gamma$  interaction takes the following form [42]:

$$iL_{eff}^{WW\gamma} = iL_{eff(1)}^{WW\gamma} + iL_{eff(2)}^{WW\gamma} + iL_{eff(3)}^{WW\gamma}, \quad (2.30)$$

where

$$iL_{eff(1)}^{WW\gamma} = e[g_1^\gamma A^\mu (W_{\mu\nu}^- W^{+\nu} - W_{\mu\nu}^+ W^{-\nu}) + \kappa_\gamma W_\mu^+ W_\nu^- A^{\mu\nu} + \frac{\lambda_\gamma}{m_W^2} A^{\mu\nu} W_\nu^{+\rho} W_{\rho\mu}^-], \quad (2.31)$$

$$iL_{eff(2)}^{WW\gamma} = e[ig_5^\gamma \epsilon_{\mu\nu\rho\sigma} ((\partial^\rho W^{-\mu}) W^{+\nu} - W^{-\mu} (\partial^\rho W^{+\nu})) A^\sigma + ig_4^\gamma W_\mu^- W_\nu^+ (\partial^\mu A^\nu + \partial^\nu A^\mu)], \quad (2.32)$$

$$iL_{eff(3)}^{WW\gamma} = e[\frac{\tilde{\kappa}_\gamma}{2} W_\mu^- W_\nu^+ \epsilon^{\mu\nu\rho\sigma} A_{\rho\sigma} - \frac{\tilde{\lambda}_\gamma}{2m_W^2} W_{\rho\mu}^- W_\nu^{+\mu} \epsilon^{\nu\rho\alpha\beta} A_{\alpha\beta}], \quad (2.33)$$

where  $e$  is the absolute value of the electron charge,  $A^\mu$  is the photon field,  $W^{\pm\mu}$  are the fields of the  $W^\pm$  bosons,  $W_{\mu\nu} = \partial_\mu W_\nu - \partial_\nu W_\mu$ ,  $A_{\mu\nu} = \partial_\mu A_\nu - \partial_\nu A_\mu$ ,  $m_W$  is the mass of the  $W$  boson,  $g_1^\gamma$ ,  $\kappa_\gamma$ ,  $\lambda_\gamma$ ,  $g_5^\gamma$ ,  $g_4^\gamma$ ,  $\tilde{\kappa}_\gamma$ , and  $\tilde{\lambda}_\gamma$  are constants.

Despite seven constants in the extended Lagrangian, only  $\lambda_\gamma$  and  $\kappa_\gamma$  are considered in the aTGC searches. The rest of the constants are fixed to their SM values based on the following considerations. The constants  $g_1^\gamma = 1$  and  $g_5^\gamma = 0$  are fixed to make the Lagrangian obey the electromagnetic gauge invariance for the on-shell photons. The non-zero value of  $g_4^\gamma$  also violates C and P conserva-

tions, and non-zero values of  $g_4^\gamma$ ,  $\kappa_\gamma$ ,  $\tilde{\lambda}_\gamma$  violate the CP conservation law. Such violation parametrizations are not considered in charged TGC measurements, thus, constants  $g_4^\gamma$ ,  $\kappa_\gamma$ , and  $\tilde{\lambda}_\gamma$  are fixed to zero.

The SM values of  $\lambda_\gamma$  and  $\kappa_\gamma$  are  $\lambda_\gamma = 0$  and  $\kappa_\gamma = 1$ . For convenience, the deviation from the SM value is introduced  $\Delta\kappa_\gamma \equiv \kappa_\gamma - 1$ . These two parameters are tested in  $WW\gamma$  aTGC searches because non-zero values of these parameters would not violate any fundamental law.

The most significant effects of aTGC would appear at high energy scales. Figure 2.5 shows this effect in  $P_T^\gamma$  spectrum of 7 TeV  $W\gamma \rightarrow \mu\nu\gamma$  measurement. As seen in Fig. 2.5, the spectrum with non-zero values of aTGC constants at low  $P_T^\gamma$  coincides with the SM prediction but for higher  $P_T^\gamma$  the disagreement appears.

A common approach to aTGC searches is to measure the spectrum of a kinematic parameter highly correlated with the energy of a final state particle or a system of final state particles. For  $W\gamma$  process, the most sensitive variable is  $P_T^\gamma$ . Examining this spectrum allows us to probe and constrain aTGC coupling constants. Chapter 2.5 reviews the experimental results to date on constraining aTGC coupling constants of the  $WW\gamma$  vertex.

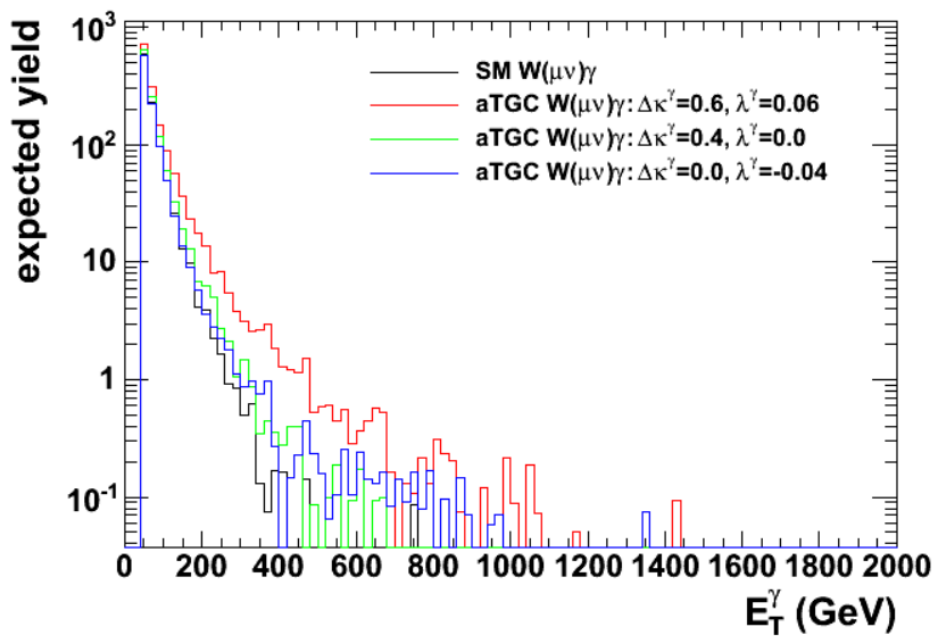


Figure 2.5: Distributions of  $P_T^\gamma$  in simulated  $W\gamma \rightarrow \mu\nu\gamma$  events with different values of aTGC constants at LHC energy of  $\sqrt{s} = 7$  TeV. Source of figure: [40].

## 2.5 A brief history of $W\gamma$ measurements

aTGC parameters of the  $WW\gamma$  vertex can be probed in measurements of  $W\gamma$ ,  $WW$ ,  $WZ$  processes. Limits on the  $\Delta\kappa_\gamma$  and  $\lambda_\gamma$  constants obtained by different experiments are summarized in Fig. 2.6. The summary includes the combination results from Do [13] and LEP [22] as well as results of several individual measurements by ATLAS and CMS including  $W\gamma$  at  $\sqrt{s} = 7$  TeV [35], [36],  $WW$  at  $\sqrt{s} = 7$  and 8 TeV [37], [8], [9], and  $WV$  at  $\sqrt{s} = 7$  and 8 TeV [2], [7] measurements.

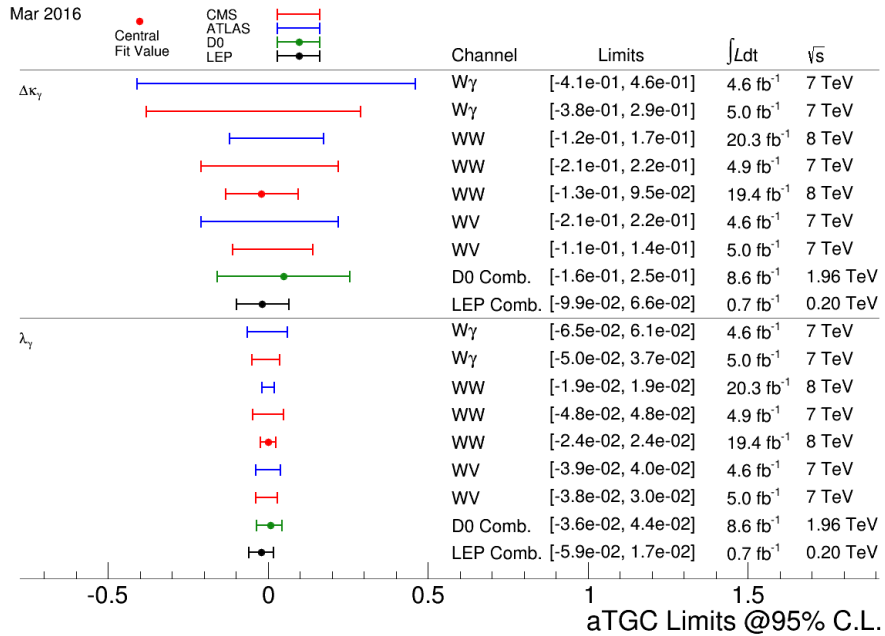


Figure 2.6: Summary of limits on the  $WW\gamma$  aTGC coupling constants. Figure from [46].

The most recent measurements of  $W\gamma$  production were performed by CMS [36] and ATLAS [35] collaborations with  $pp$  collisions at  $\sqrt{s} = 7$  GeV collected in 2011. Both collaborations considered two channels:  $W\gamma \rightarrow \mu\nu\gamma$  and  $W\gamma \rightarrow e\nu\gamma$ .

Diboson processes are rare in  $pp$ -collisions and analysts have to filter out events of their interest from many processes which are more likely to happen. To do

that, a variety of selection criteria are applied which reject most of the background events to increase the signal fraction in the selected sample as much as possible. However, even after all possible selection criteria are applied, the majority of selected events are still background events and it is not possible to reduce the background any further without also significantly reducing signal.

The major source of such irreducible background is the fake photon background where hadronic jets are misidentified as photons. Such events originate mostly from  $W+jets$ , but  $Z+jets$  and  $t\bar{t}+jets$  events contribute to this source of background as well. In the electron channel there is one more significant background that is the fake photon background where electron is misidentified as a photon. Such events are coming from  $Z+jets$  events. For the muon channels this background is small. Other sources of backgrounds for both channels include real- $\gamma$ , fake lepton + real photon and fake lepton + fake photon backgrounds. The major source of real- $\gamma$  background is the  $Z\gamma$  process where a final state lepton and a photon mimics the  $W\gamma$  final state. Fake lepton + real photon background originates from the  $\gamma+jets$  process where a jet is misidentified as a lepton. Fake lepton + fake photon backgrounds come from dijet and multijet events where one of the jets is misidentified as a lepton and the other one is misidentified as a photon. The probability of a jet to be misidentified as a lepton is very small, therefore fake lepton + real photon and fake lepton + fake photon backgrounds are negligible.

$P_T^\gamma$  spectra are measured because this variable is the most sensitive to the potential aTGC. The  $P_T^\gamma$  spectra of the selected events in data superimposed with selected events in the simulation of the signal and estimated background contribution for the muon and electron channels are shown in Fig. 2.7 for CMS and in Fig. 2.8 for ATLAS measurement. Both measurements show a good agreement between data and the simulation.

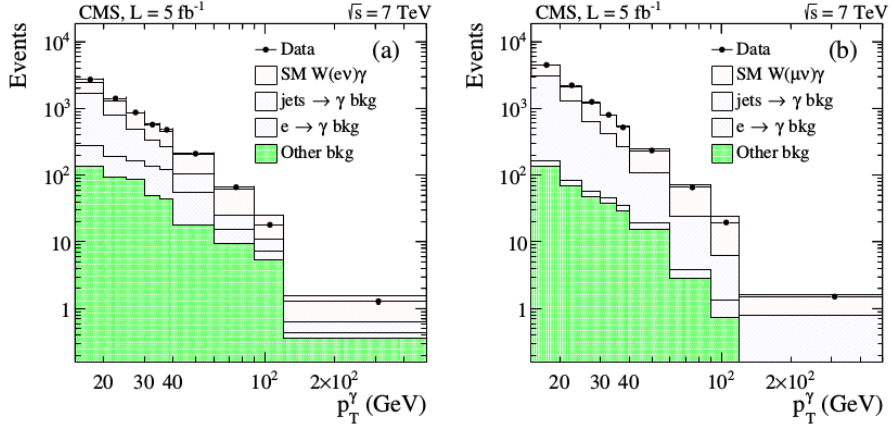


Figure 2.7: The distribution of the  $p_T^\gamma$  of  $W\gamma$  candidates in the analysis of 7 TeV CMS data. Data vs signal MC + background estimates. Left:  $W\gamma \rightarrow e\nu\gamma$ , right:  $W\gamma \rightarrow \mu\nu\gamma$  [36].

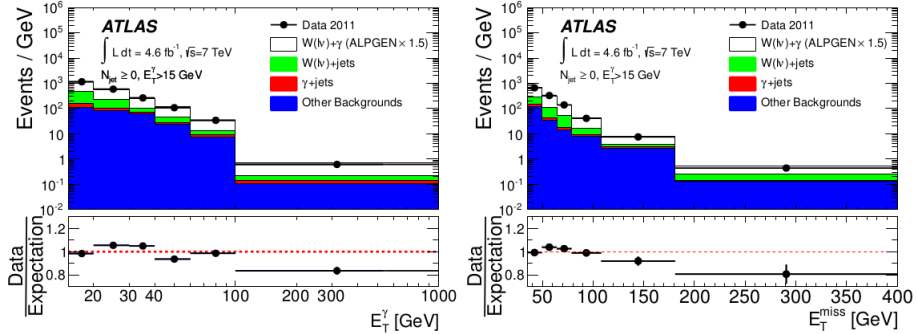


Figure 2.8: The distribution of the photon transverse momentum (left) and missing transverse momentum (right) of  $W\gamma$  candidates in the analysis of 7 TeV ATLAS data. Data vs signal MC + background estimates [35].

The phase space restrictions of  $W\gamma$  measurements come from the considerations of the detector acceptance, reducing heavily background-dominated regions and theoretical considerations such as to avoid divergence of the cross section and to reduce ISR and FSR contributions to the cross section.

CMS provides measurements of the  $P_T^\gamma$  spectrum, the total cross section within the phase spaces of  $\Delta R > 0.7$ ,  $P_T^\gamma > 15$  GeV,  $P_T^\gamma > 60$  GeV and  $P_T^\gamma > 90$  GeV.

ATLAS, in addition to the  $P_T^\gamma$  spectrum, total cross section and limits, provides the differential cross section and cross section with different number of associated jets. The phase space restrictions for ATLAS measurement include requirements on charged lepton kinematics  $P_T^l > 25$  GeV,  $|\eta_l| < 2.47$ , requirements on the transverse momentum of a neutrino  $P_T^\nu > 35$  GeV, photon kinematics  $P_T^\gamma > 15$  GeV,  $|\eta^\gamma| < 2.37$ , photon isolation fraction  $\epsilon_h^P < 0.5$  and lepton-photon separation  $\Delta R(l, \gamma) > 0.7$ . For the differential cross section in number of associated jets, the requirements on jets kinematics and jets separation from leptons and photons are also applied:  $E_T^{jet} > 30$  GeV,  $|\eta^{jet}| < 4.4$ ,  $\Delta R(e/\mu/\gamma, jet) > 0.3$ . No evidence of new physics is observed.

The estimated cross sections with any number of associated jets for  $P_T^\gamma > 15$  GeV are

$$\sigma(pp \rightarrow W\gamma \rightarrow l\nu\gamma) = 37.0 \pm 0.8 \text{ (stat.)} \pm 4.0 \text{ (syst.)} \pm 0.8 \text{ (lumi.) pb} \quad (2.34)$$

and

$$\sigma(pp \rightarrow W\gamma \rightarrow l\nu\gamma) = 2.77 \pm 0.03 \text{ (stat.)} \pm 0.33 \text{ (syst.)} \pm 0.14 \text{ (lumi.) pb} \quad (2.35)$$

for CMS and ATLAS respectively. The results agree with NLO MCFM [28] predictions of  $31.81 \pm 1.8$  pb for the phase space used by CMS and of  $1.96 \pm 0.17$  pb for the phase space used by ATLAS.

In addition to the cross sections, both CMS and ATLAS provide limits on aTGC coupling constants  $\Delta\kappa_\gamma$  and  $\lambda_\gamma$ . To do that, samples with non-zero aTGC coupling

constants are generated, run through the whole reconstruction and selection procedures, and compared to the measured results of  $P_T^\gamma$  spectra. The results on one-dimensional limits are quoted in Fig. 2.6 while the results on two-dimensional limits can be found in [35], [36].

In this dissertation we are measuring total and differential  $d\sigma/dP_T^\gamma$  cross section. While the aTGC limits are not derived in this dissertation, the measured differential cross section can be used to derive them. The measurement details and results are described in Chapter 5.

# Chapter 3

## Experimental Setup

Some general intro about LHC and CMS

### 3.1 Large Hadron Collider

The Large Hadron Collider (LHC) [23], [25], [26] is the largest particle accelerator and the most ambitious particle physics research facility ever built. The LHC accelerates two particle beams up to the speed close to the speed of light. The beams travel in opposite directions, each in its own beam pipe, in ultrahigh vacuum. Beam structure is bunches of a large number of charged hadrons. The bunches are accelerated by varying electromagnetic fields, are focused by superconducting quadrupole magnets and steered by dipole magnets. The bunches collide at the collision points where particle detectors are placed. New particles are produced in the collisions and registered by the detectors for various BSM searches as well as precision SM measurements.

The LHC is placed into a tunnel originally built for the LEP accelerator. The LEP was decommissioned to make room for the LHC. The tunnel is about 27 km in circumference, located at the Swiss-French boundary up to 100 meters underground.

Before entering LHC, particle beams are going through several stages of the acceleration and the LHC is the last element of the chain of the CERN's accelerator complex (Fig. 3.1). Protons are extracted from hydrogen atoms, are accelerated by Linac2 to energies of 5 MeV, then injected into the Proton Synchrotron Booster (PSB) where they reach energies of 1.4 GeV. After that protons are sent to PS and Super PS (SPS) where they are accelerated up to 25 GeV and 450 GeV respectively. Finally, protons enter the LHC and are accelerated to reach their collision energies of several TeV per beam. Besides protons, the complex also accelerates and collides lead ions however in this dissertation we analyze data from proton-proton collisions only and, therefore, are not discussing lead ion collisions.

## CERN's Accelerator Complex

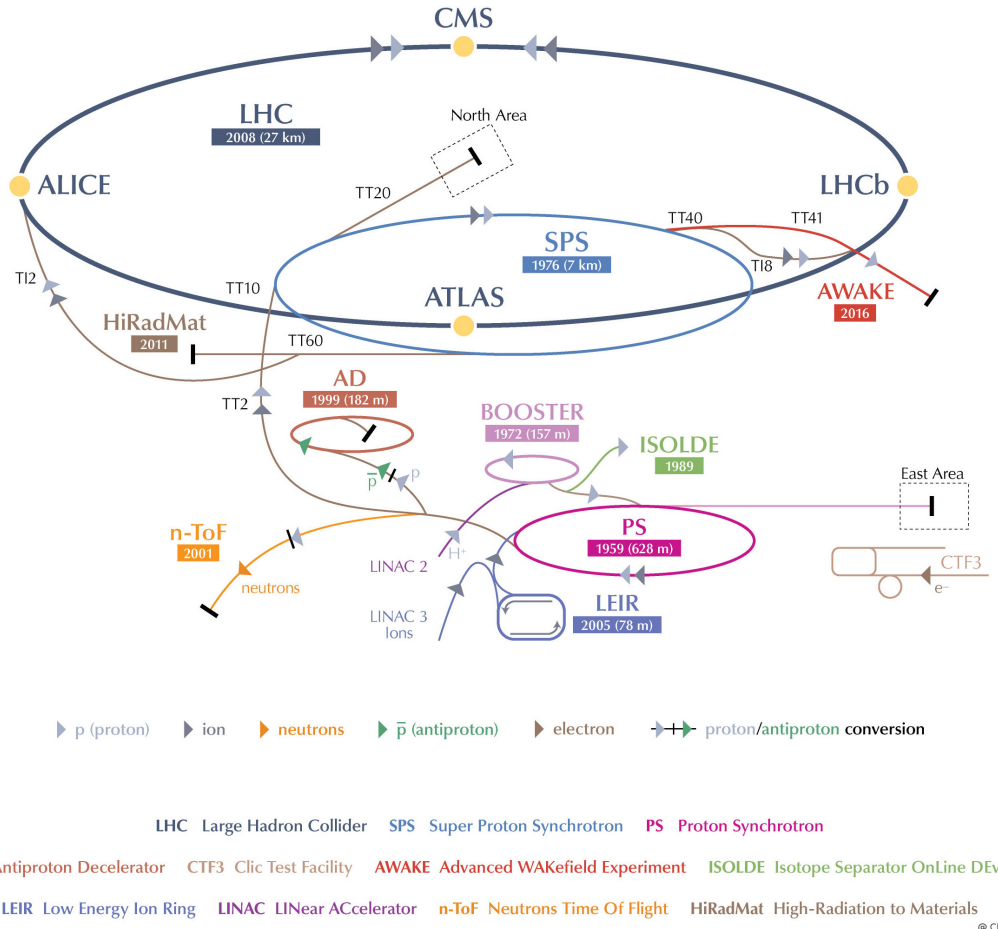


Figure 3.1: CERN's accelerator complex [14].

Six detectors are installed at the LHC to detect products of hadron collisions and to perform measurements of the LHC physics program. There are general purpose detectors ATLAS and CMS, there is LHCb which specializes on the physics of B-mesons, and ALICE which is designed to detect products of heavy ion collisions. In addition, there are two relatively small detectors: LHCf and TOTEM which are installed close to the ATLAS and CMS collision points respectively. The greatest

achievement by the LHC today is the discovery of the Higgs boson in 2012 by the CMS [11] and the ATLAS [10] collaborations.

The design energy of the LHC is 7 TeV per beam however it is taking years to reach the design energy, and, meanwhile, several lower energy points were and are being probed. In 2010-2011 the LHC operated at energy of 3.5 TeV per beam which was already higher than energy of any other collider. In 2012 the energy increased up to 4 GeV. In 2013-2014 the LHC was shut down for upgrades. Collisions were restarted at 6.5 TeV in 2015 and continued at this energy in 2016.

All important measurements performed at lower energies are also repeated at higher energies because the ability to probe higher energy scales increases our chances for a discovery and even if no deviations from the known physics are found at a given energy point, the discovery is still possible to happen as we go higher in the energy. Precision SM measurements of cross section need to be done at all energies and compared to theory since the cross sections evolve with energy. The cross sections of many interesting processes increase with energy because in collision of higher energy hadrons more partons are able to participate in the interactions. Thus, more rare processes can be explored. Cross sections of various productions in  $pp$  collisions and their energy dependencies are shown in Fig. 3.2.

In addition to the beam energy, there are many other collider parameters. A brief summary of them is available in Tab. 3.1. One of the most important parameters of an accelerator is the ability to produce a large number of interesting collisions which is determined by the luminosity (Ch. 2.2). The instantaneous luminosity is determined by the following expression [31]:

$$L = f \frac{n_1 n_2}{4\pi\sigma_x\sigma_y} \quad (3.1)$$

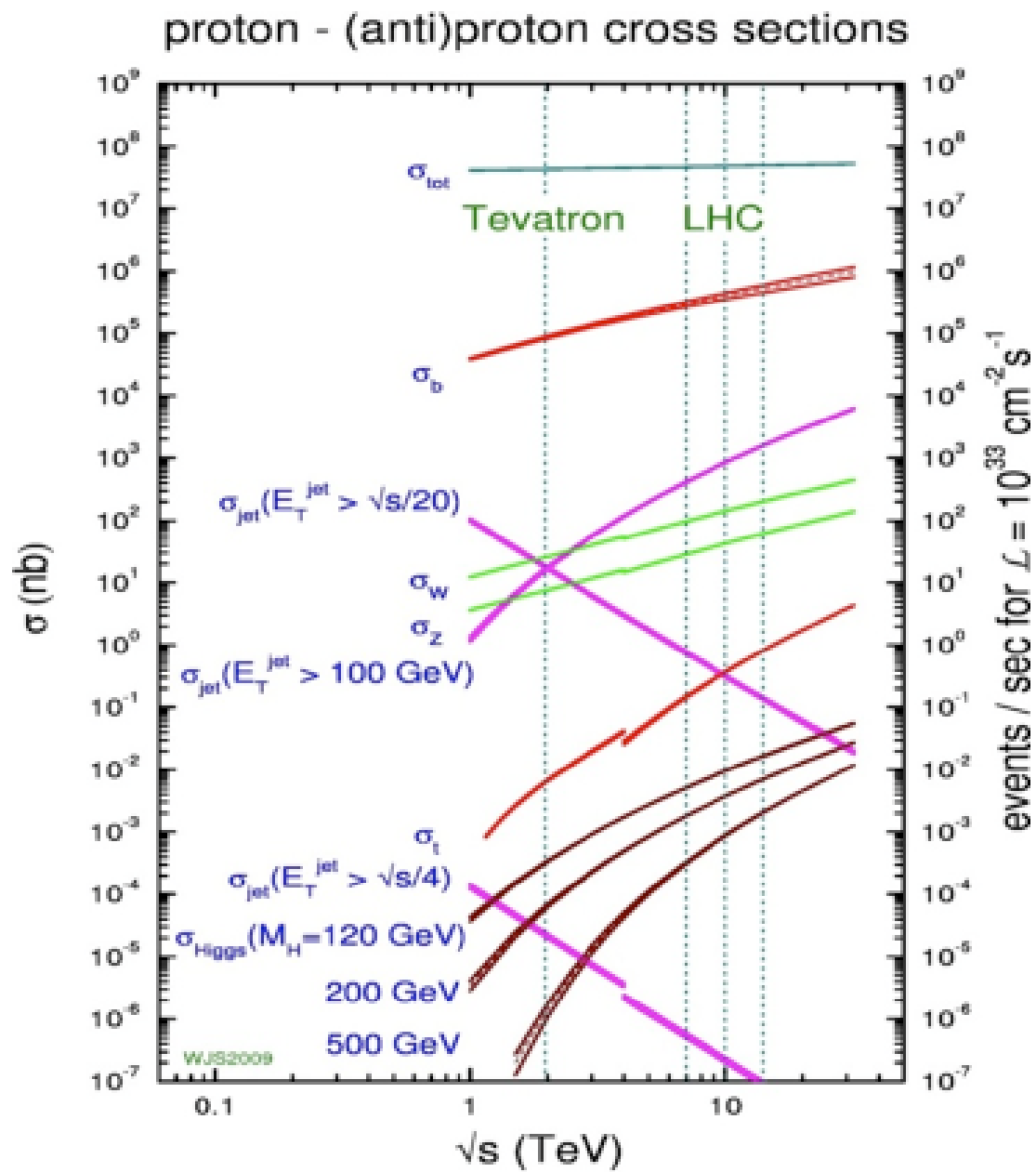


Figure 3.2: Cross sections of various productions in  $pp$  collisions [39].

where  $n_1$  and  $n_2$  are numbers of particles in colliding bunches,  $f$  is a frequency of collisions,  $\sigma_x$  and  $\sigma_y$  characterize sizes of overlapping parts of colliding beams in horizontal and vertical directions. Instantaneous luminosity multiplied by a cross section of a process gives an event rate (Eq. 2.26). To determine the integrated luminosity, one has to integrate the instantaneous luminosity over time:

$$L_{int} = \int L dt \quad (3.2)$$

With the integrated luminosity one can compute the total number of events of interest over the full period of data collection, thus the integrated luminosity of a data sample is a measure of the size of the data sample.

The luminosity of the LHC is also higher than of any previously existed collider. The integrated luminosity of the LHC for  $pp$  collisions for different years of the operation is shown in Fig. 3.3. Run periods of LHC in 2010-2012 refer to Run I of the LHC operation. While working on energy of  $\sqrt{s} = 7$  TeV, LHC delivered  $45 \text{ pb}^{-1}$  and  $6.1 \text{ fb}^{-1}$  of data in 2010 and 2011 year respectively. In 2012 the working energy of LHC was  $\sqrt{s} = 8$  TeV, and the integrated luminosity was  $L_{int} = 23.3 \text{ fb}^{-1}$ . After a long shutdown, LHC was upgraded for Run II, to operate on  $\sqrt{s} = 13$  TeV in 2015 and delivered  $4.2 \text{ fb}^{-1}$  of data by the end of 2015. In 2016 LHC continued operating at  $\sqrt{s} = 13$  TeV and delivered the integrated luminosity of  $41.1 \text{ fb}^{-1}$  [24].

The measurement of this dissertation is performed at the energy of 4 TeV per beam or at the center of mass energy  $\sqrt{s} = 8$  TeV with  $19.6 \text{ fb}^{-1}$  of data. The same process was measured at  $\sqrt{s} = 7$  TeV with about four times less amount of data by both CMS and ATLAS. These measurements are discussed in greater details in Ch. 2.5.

Table 3.1: Main parameters of LHC [23]

Circumference	27 km
Dipole operating temperature	1.9 K
Number of magnets	9593
Number of main dipoles	1232
Number of main quadrupoles	392
Number of RF cavities	8 per beam
Nominal energy, protons	7 TeV
Nominal energy, lead ions	2.76 TeV per nucleon
Peak magnetic dipole field	8.33 T
Min. distance between bunches	7 m
Design luminosity	$10^{34} \text{ cm}^{-2} \text{ s}^{-1}$
No. of bunches per proton beam	2808
No. of protons per bunch (at start)	$1.1 \times 10^{11}$
No. of collisions per second	600 millions

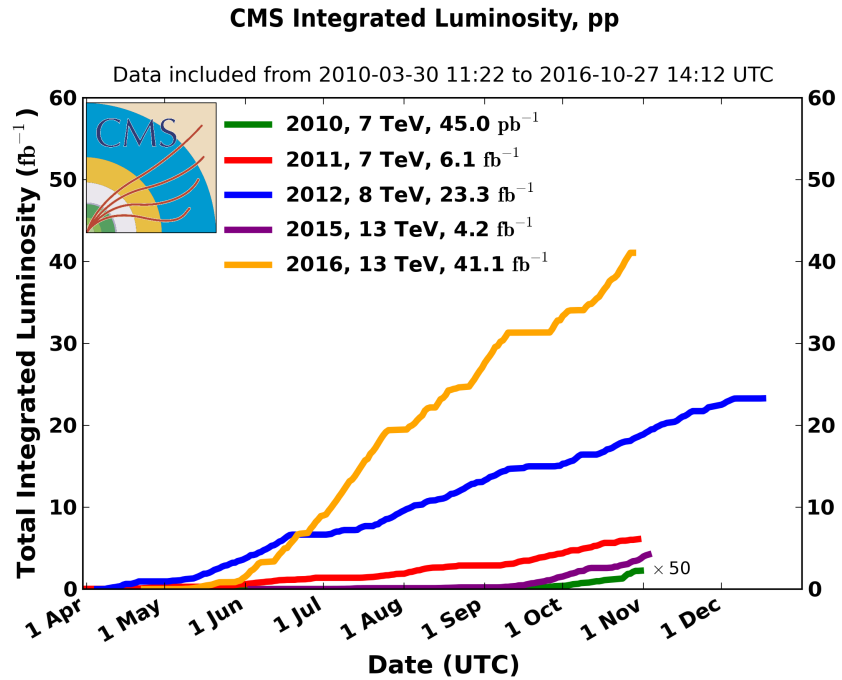


Figure 3.3: LHC integrated luminosity by year [15].

## 3.2 Compact Muon Solenoid

### 3.2.1 Introduction

The CMS is a general-purpose detector designed for detecting various highly energetic particles which are being produced in  $pp$  collisions at the LHC [3]. The CMS has a broad program with goals of direct and indirect searches of the BSM physics including but not limited to supersymmetric particles as well as precision measurements of various SM parameters.

The CMS detector is a cylindrically symmetric with a colliding beam as a central axis. Cartesian, cylindrical and spherical coordinates are all used to describe the CMS geometry, depending on the context. The  $x$ -axis of the CMS points towards the center of the LHC while the  $y$ -axis points vertically up. The direction of the  $z$ -axis corresponds to the counterclockwise direction of the LHC beam (Fig. 3.4, left). Cylindrical coordinates are defined as  $r = \sqrt{x^2 + y^2}$ ,  $\phi = \arctan(y/x)$ . Instead of the polar angle  $\theta$ , it is more convenient to use the pseudorapidity  $\eta = -\ln \tan \theta/2$ . A pseudorapidity ranges from  $\eta = -\infty$  to  $\eta = +\infty$  for directions parallel to the beam axis with the value of  $\eta = 0$  for a direction perpendicular to the beamline. This variable is convenient for measurements because a distribution of a massless particle in  $\eta$  is nearly flat. The acceptance of the CMS in  $\eta$  is limited and varies from  $|\eta| < 2.4$  to  $|\eta| < 5.3$  depending on a subdetector (Fig. 3.7, top).

The detector consists, from inner to outer layer, of a tracking system, an electromagnetic calorimeter (ECal), a hadronic calorimeter (HCal), a magnet and a muon system. Having the tracking system, ECal and HCal inside of a large solenoid makes the detector compact. A segment of a CMS slice in  $r - \phi$  plane is shown in Fig. 3.5.

When a heavy particle is produced in a collision, it decays immediately, and

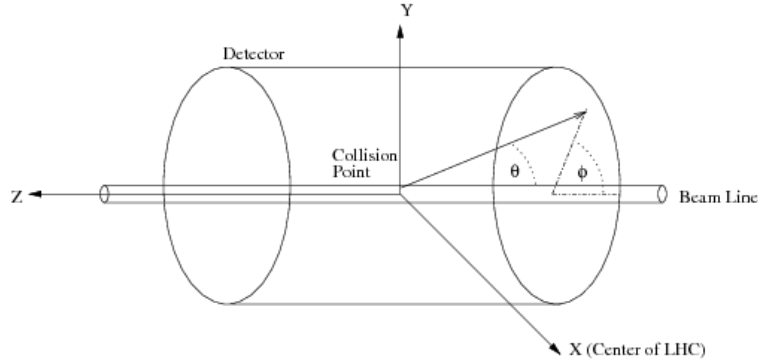


Figure 3.4: CMS coordinate system.

we detect its long-living decay products including an electron, a photon, a muon, a neutral hadron or a charged hadron. Depending on the trace left by a particle in different subdetectors we can identify a particle. Electrons and positrons leave curved tracks, trajectories of charged particles, in the tracking system and then induce showers in the electromagnetic calorimeter (ECal). Photons induce the same electromagnetic showers in ECal however, as neutral particles, they do not leave tracks in the tracking system. Hadrons normally travel through the ECal undisturbed and induce a hadronic shower in the hadronic calorimeter (HCal). Charged and neutral hadrons can be distinguished from each other by checking whether they leave a track in the tracking system or not. Muons are the only particles which penetrate through the ECal, the HCal and the magnet and leave tracks in the CMS muon system. Neutrinos are not detected by CMS.

All subdetectors are important for the  $W\gamma$  measurement and the remainder of this chapter describes the subdetectors in greater details. Muons and electrons which we have as final state particles are both affected by CMS magnetic field allowing the tracking system and the muon system to measure their trajectory parameters and momenta. In this dissertation we use the information of the

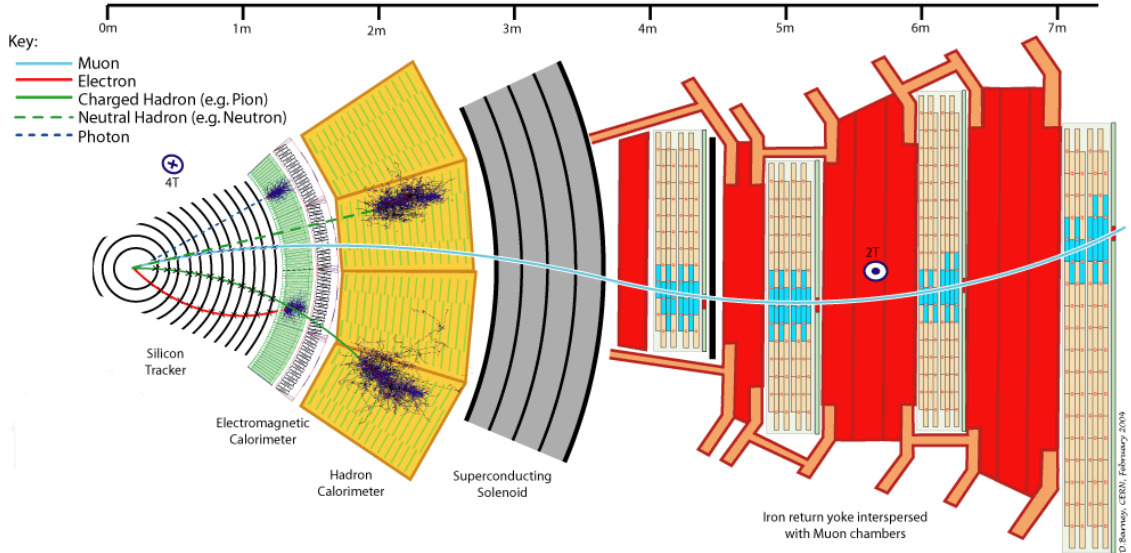


Figure 3.5: CMS slice.

primary vertex, the collision point, determined by the tracking system to select our events. Also the tracker provide us the information about electrons trajectories and momenta in the electron channel and distinguishes between electrons and photons. The ECal is necessary to identify electrons and photons and to measure all kinematic parameters of photon. The HCal is also used for electrons and photons identification: the energy deposit in the HCal left by an electron or a photon must be very small compared to the energy deposit left in the ECal. The muon system is essential for muon reconstruction and identification.

### 3.2.2 Magnet

A magnetic field in a particle detector is necessary to measure momenta of charged particles by track curvatures. The higher the momentum is, the less a particle trajectory is affected by the magnetic field. In CMS momenta of all charged particles are measured in the tracking system. In addition, momenta of muons are

measured in the muon system.

The CMS magnet is placed between layers of HCal and a muon system. The magnet is made of superconducting wires. An electric current flowing in the wires creates a uniform field of  $B = 4\text{T}$  inside the solenoid, for the tracking system, and also provides a smaller magnetic field of a certain configuration outside the solenoid, for the muon system. Stronger field in the tracking system is necessary because of higher track density and a smaller size than those in the muon system.

### 3.2.3 Tracking System

The tracking system measures track geometry including particles trajectories and locations of primary and secondary vertices and momenta of charged particles. It needs to disturb particles as little as possible so that they can pass through. Therefore, just a few measurements must be enough to reconstruct the track. The accuracy of a measurement of each hit, position measurement, is  $10\text{ }\mu\text{m}$ .

The tracking system consists of silicon pixels and silicon strips (Fig. 3.6). Tracks that originate from proton collisions, collision tracks, start at the center and then cross the layers of the tracking system. Tracks are straight in  $r - z$  plane and curved by the magnetic field in the  $r - \phi$  plane. The acceptance of the tracker system in  $r - z$  plane is geometrically limited by the absolute value of the pseudorapidity  $|\eta| = 2.5$ .

The pixel tracker is the closest subsystem of CMS to the collision point thus it experiences the largest particle flux: at 8 cm from the collision point the flux is about 10 million  $1/(\text{cm}^2\text{s})$ , and the pixel detector with its 65 millions sensors is capable to reconstruct all these tracks. It consists of three layers of cylinders in the barrel with radii of 4 cm, 7 cm and 11 cm which are referred as pixel barrel (BPIX)

and four disks in the endcap, two disks at each side, which are referred as pixel forward (FPIX).

The strip tracker is placed right after the pixel tracker and occupies the detector volume up to 130 cm around the beam axis. The strip tracker consists of four parts: the tracker inner barrel (TIB), the tracker inner disks (TID), the tracker outer barrel (TOB) and the tracker endcap (TEC) as shown in Fig. 3.6. In the strip tracker there are over 15,000 sensitive modules with a total number of 10 million strips. Each sensitive module consists of a set of sensors, its support structure and readout elements.

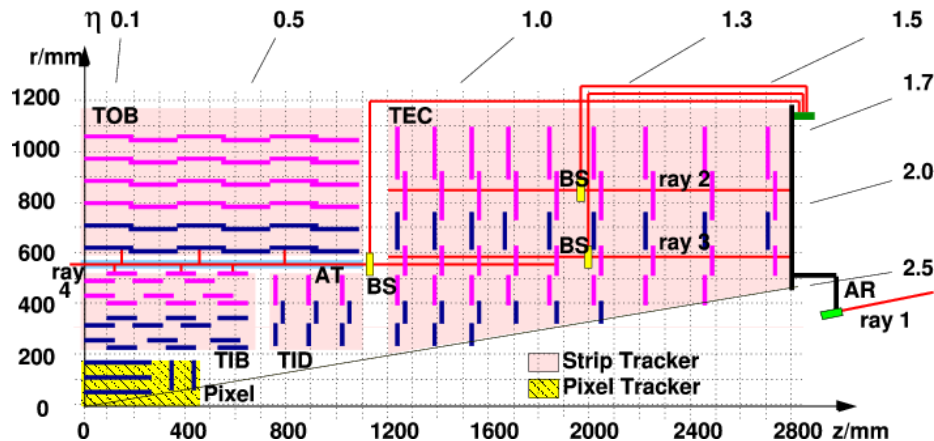


Figure 3.6: Slice of the CMS tracking system in  $r - z$  plane.

### 3.2.4 Electromagnetic Calorimeter

The ECal is a layer between the tracking system and the HCal. It is made of high-density lead tungstate crystals arranged in a barrel section and two endcap sections. The crystals work as scintillators. When electrons and photons pass through it, scintillators produce light proportional to the particle's energy. The

scintillated light then is amplified by photomultipliers. After that, signals are digitized and taken away by fibre optic cables.

The ECal measures energy of electrons and photons and parameters of their trajectories. To distinguish between electrons and photons, it is necessary to perform matching to the track in the tracking system. If there is a track, then there is an electron (or positron). If there is no track, then the particle is a photon.

It is important for the ECal to be able to distinguish between high energetic photons and pairs of lower energetic photons e.g. from a  $\pi^0$  decay. It is especially difficult in the endcap sections where angle between two photon trajectories is small. For this reason, ECal preshower which have 15 times smaller granularity are located in front of the endcaps. The preshower provide extra spacial precision.

### 3.2.5 Hadron Calorimeter

The HCal measures the energy of charged and neutral hadrons. Also it plays a key role in indirect detection of invisible particles like neutrinos.

Invisible particles leaves no record in CMS detector. They are detected by missing transverse energy ( $E_T^{miss}$ ) that is determined as

$$E_T^{miss} = - \sum P_T, \quad (3.3)$$

where the summation covers all visible particles in the event. Therefore, for precise measurement of  $E_T^{miss}$  it is important to capture the full energy release of all visible particles. For this purpose, HCal is designed to stop all hadrons passing through.

The HCal consists of barrel, endcap and forward parts. Its acceptance extends to  $|\eta| = 3.0$  for endcaps and to  $|\eta| = 5.3$  for forward HCal.

The HCal is a sampling calorimeter, it consists of alternating layers of absorbers

and scintillators. When a hadron hits an absorber, it induces a hadronic shower. The light produced by the shower is collected on optic fibres and passed to the readout system. The total amount of light collected from a certain region of the HCal is a measure of hadron's energy. In addition to the energy, the HCal also reconstructs trajectory of the hadron.

### 3.2.6 Muon System

Muons pass through the ECal, the HCal and the magnet without interacting. They are the only particles that are registered in the muon system which is placed outside the magnet and which is the largest part of CMS detector.

There are four concentric layers of muon detectors (stations) and iron return yoke between them. Muons induce several hits in the muon stations which are later fitted and matched to the tracking system measurements to provide the best possible resolution in the measurements of all parameters of the muon's trajectory and momentum.

There are three types of muon chambers used in the CMS muon system: drift tubes (DTs), cathode strip chambers (CSCs) and resistive plate chambers (RPCs). Overall, there are 1400 muon chambers including 250 DTs, 540 CSCs and 610 RPCs.

The system of DTs measures positions of muons in the barrel. Each DT chamber is about 2 m by 2.5 m in size. It consists of 12 layers of aluminium which are arranged as groups of four. There are up to 60 drift tubes in a layer. The middle group of layers measures z-coordinate and two other groups determine the perpendicular coordinate.

Each drift tube is 4 cm in width, is filled with a gas and has a wire inside. When a charged particle passes through the volume, it ionizes atoms and the wire

receives an electric charge.

CSCs are placed in endcap regions. CSCs are arrays of anode wires crossed by copper cathode strips placed in a gas volume. When a charged particle penetrates the gas volume, it ionizes the gas. Electrons drift to the wires while ions move to the strips. Strips are perpendicular to wires, thus, we measure two coordinates for each particle.

RPCs are parallel capacitors made of high-resistivity plastic plates with a space between them filled with a gas. RPCs provide quick measurements of muon momenta and are used for triggering.

### 3.2.7 Triggering and Data Aquisition

At peak luminosity, CMS experiences one billion proton-proton collisions per second which come in bunches separated just by 25 ns from one other. New events come before the events from the previous bunch crossing left the detector. To process the information from many different collisions at the same time, data is stored in pipelines.

It is not technically possible to readout all these events. Moreover, we do not need most of these events for a physics measurement because most of these events do not have a potential to discover a new physics. We have resources to store about one hundred events out of one billion that is why we need a trigger system that quickly decides what the best one hundred events are.

If the triggers were too loose, and we would select one hundred events too quickly, e.g., out of a hundred million events, then CMS would not be able to process the rest 90% of events in a given set of one billion and we would lose 90% of potentially interesting events.

If the triggers were too strict, we would select, e.g., ten events out of one billion, not one hundred and lose CMS potential to store and process data by 90% which would significantly reduce our chances for a discovery.

Thus, the challenge of the trigger system is to select the best one hundred events out of one billion and do that fast to be able to process every single event. To achieve this goal, a two-level trigger system was developed consisting from the Level 1 trigger (L1T) and the high level trigger (HLT) as shown in Fig. 3.9.

L1T is a hardware based trigger (Fig. 3.10). It uses information from the ECal, HCal and muon system. L1T reduces frequency of coming events from 40 MHz to 100 kHz. Events that did not pass the L1T are lost forever while events that pass the L1T are temporarily stored to get checked by the HLT.

HLT is a software-based trigger. It uses information from all subdetectors and runs quick reconstruction and identification algorithms to determine types of particles and their kinematics. It reduces the number of events to 100 Hz. Events that did not pass HLT are lost forever. Events that pass HLT are arranged into appropriate datasets depending on HLT selection criteria they passed and stored for physics analyses.

### 3.2.8 Particle Flow Algorithm of Event Reconstruction

A particle flow algorithm is used by CMS to identify and reconstruct stable particles [32]. It processes the information from all CMS subdetectors and identifies and reconstructs each stable particle in an event individually. The list of particles include muons, electrons, photons, charged and neutral hadrons. Each type of particles leaves its own trace in CMS subdetectors as shown in Fig. 3.5. After reconstruction of individual stable particles, jets are built, missing transverse

energy  $E_T^{miss}$  is determined, certain short-lived particles are reconstructed based on the list of individual stable particles in the event.

One particle can induce several different particle-flow elements in different subdetectors. The linking algorithm links these elements together producing blocks of elements. Usually there are from one to three elements in each block. Links can be connections between the tracking system and silicon strip pre-shower (PS), ECal or HCal, between PS and ECal, between ECal and HCal, and between a tracking system and a muon system.

In each block, muons are considered first. A link between charged tracks in the tracking and muon systems comprise a global muon which produces one “particle-flow muon”. The corresponding track in the tracking system is removed from the block and corresponding energy deposits are subtracted from ECal and HCal. Then electrons are reconstructed and identified using tracking system and ECal. The corresponding tracks and ECal clusters are removed from the block. Remaining tracks and clusters are considered more carefully to identify charged hadrons, neutral hadrons, and photons.

When all particles in the event are reconstructed and identified,  $E_T^{miss}$  is determined as

$$E_T^{miss} = - \sum P_T, \quad (3.4)$$

where the summation covers all visible particles in the event.  $E_T^{miss}$  is used in physics analyses as a measure of  $P_T$  of neutrinos and other invisible particles in the event. Fake  $E_T^{miss}$  can originate from particles that did not fall into the detector acceptance, particles with very high track curvature that they did not reach the tracking system, momenta mismeasurement, particle misidentification, cosmic rays

particles, and machine background.

In the measurement of this dissertation particle flow muons, electrons, photons, and  $E_T^{miss}$  are used for all the major steps of the cross section measurement including event selection, background subtraction, various corrections, and determination of phase space restrictions and bin boundaries. Each step is described in greater details in Ch. 5.

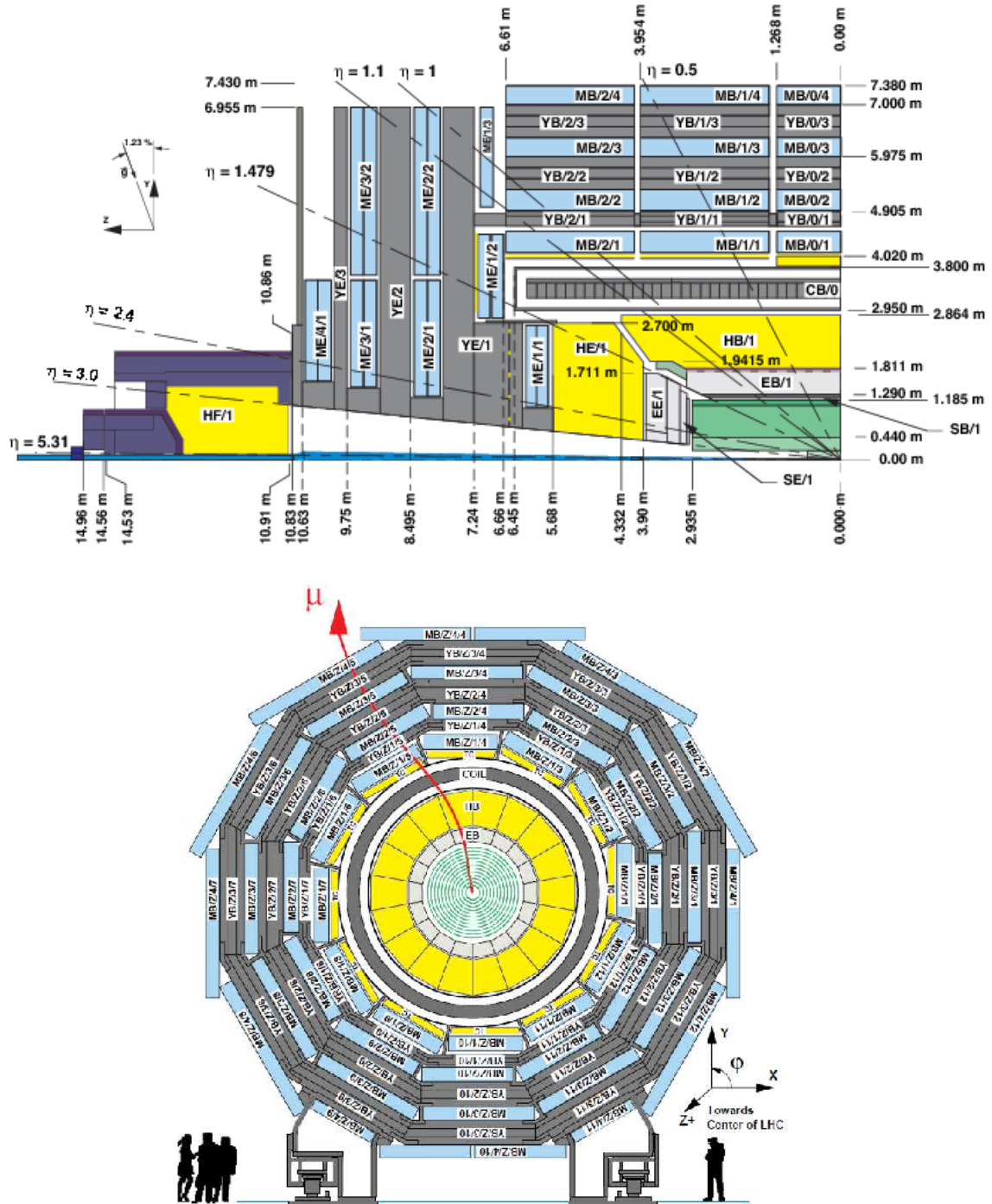


Figure 3.7: CMS detector, schematic view. Top:  $r-z$  plane, bottom:  $r-\phi$  plane at  $z = 0$  [6].

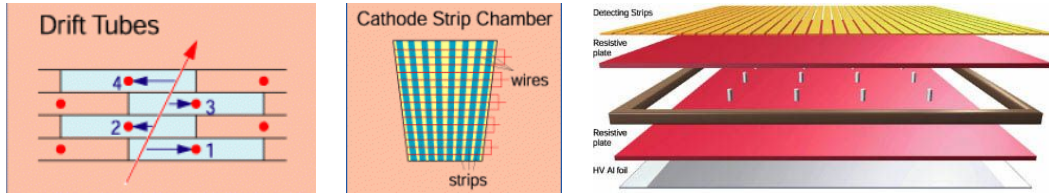


Figure 3.8: Components of the CMS muon system. Left to right: drift tubes, cathode strip chambers (CSCs), resistive plate chambers (RPCs).

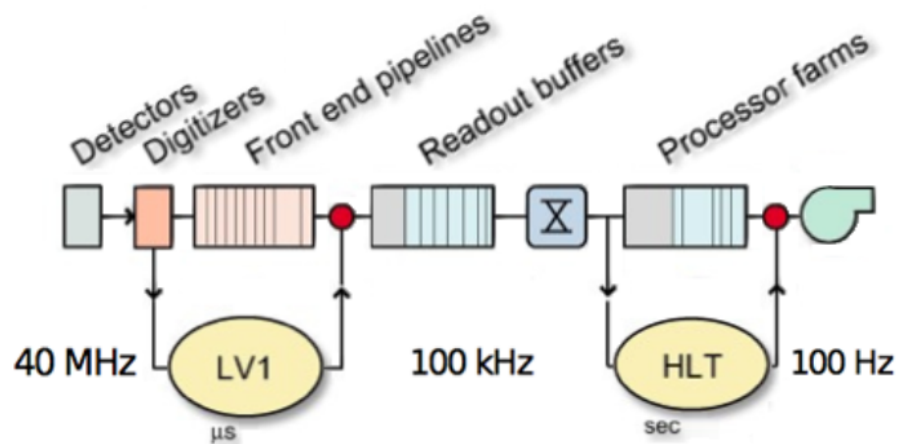


Figure 3.9: Two-level CMS trigger system.

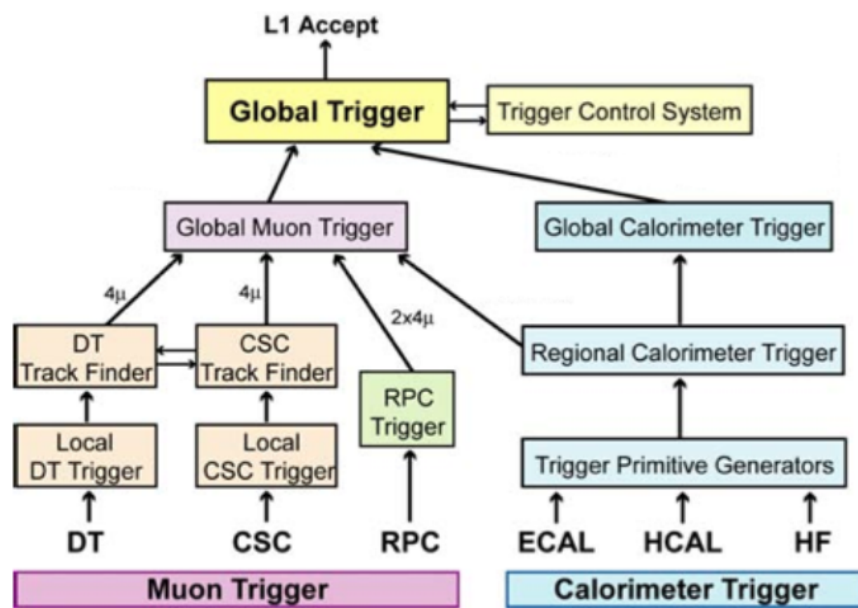


Figure 3.10: Level 1 CMS trigger system.

# Chapter 4

## CMS Tracker Alignment

A tracking system detects hits produced by a charged particle traveling through the detector that allows to reconstruct the full geometry of track as well as to determine a particle momentum. In a presence of a constant magnetic field the particle has a helical trajectory. A reconstruction algorithm determines the track parameters by fitting the positions of hits assuming the helical trajectory which can be defined by five parameters.

High precision track reconstruction is essential for particle identification and accurate measurements of particle kinematics. Smaller hit resolution and location uncertainty lead to higher precision of a measurement of the track parameters. The location uncertainty depends on our knowledge of the positions and orientations in space of the tracking system modules. The hit resolution in the CMS pixel detector is  $\sim 15 \mu\text{m}$ . When the modules are mounted, their positions are known with precision of  $\sim 200 \mu\text{m}$ . Thus, we need to know positions of modules 20 times better than they are known when mounted. The procedure of the determination of the modules locations and orientations is called the tracker alignment.

## 4.1 Approach

The concept of the track-based alignment can be illustrated in the example of the alignment of a toy tracker. When a charged particle passing through a detector (Fig. 4.1, top left) it crosses a toy tracker which consists of six flat equidistant modules (Fig. 4.1, top right). If the modules were placed exactly at their designed positions, we would observe the hits exactly at the points where the track crosses modules of ideal geometry (Fig. 4.1, middle left). However, in a reality the positions and tilts of the modules are different from ones suggested by the ideal geometry (Fig. 4.1, middle right). Hits, indeed, are recorded at the places where modules are actually mounted, not at the design ideal places (Fig. 4.1, bottom left). If we assumed a tracker to be ideal and a track to be smooth, we would see that our hits are off-track (Fig. 4.1, bottom right). So, we recalculate positions of the modules so that all the hits are laying on the same smooth track (Fig. 4.2, top left). But these recalculated positions still do not coincide with the actual positions (Fig. 4.2, top right). Then we record more and more tracks (Fig. 4.2, middle left and right). We take into account them all and determine the alignment parameters with necessary precision (Fig. 4.2, bottom left and right) minimizing residuals between measured and predicted hits.

The tracker alignment problem is the least squared problem. The expression to minimize is the following:

$$\chi^2(\mathbf{p}, \mathbf{q}) = \sum_j^{tracks} \sum_i^{hits} \left( \frac{m_{ij} - f_{ij}(\mathbf{p}, \mathbf{q}_j)}{\sigma_{ij}} \right)^2 \quad (4.1)$$

where  $\mathbf{p}$  are parameters describing the tracker geometry,  $\mathbf{q}_j$  are parameters of the  $j^{th}$  track,  $m_{ij} - f_{ij}$  are residuals, distances between the measured hit and a position predicted by the track fit,  $\sigma_{ij}$  is the Gaussian error of the measurement.

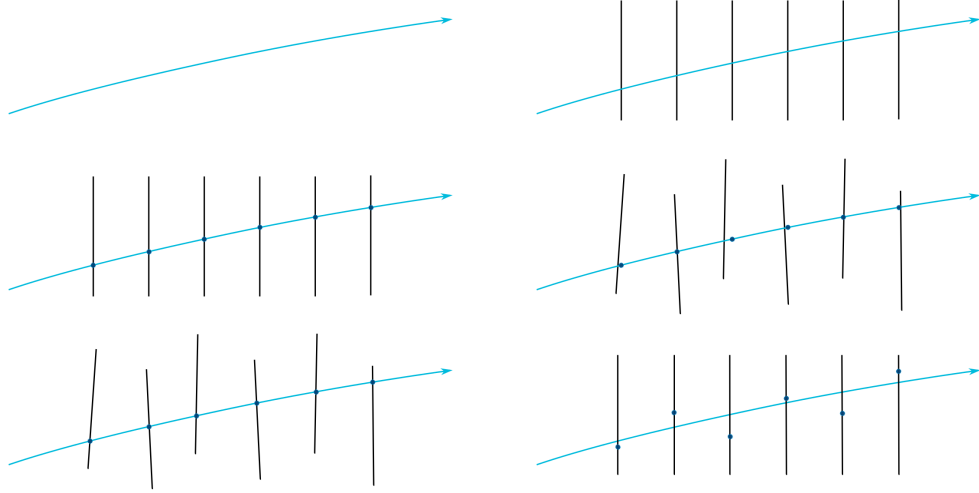


Figure 4.1: The alignment of a toy tracker, part 1.

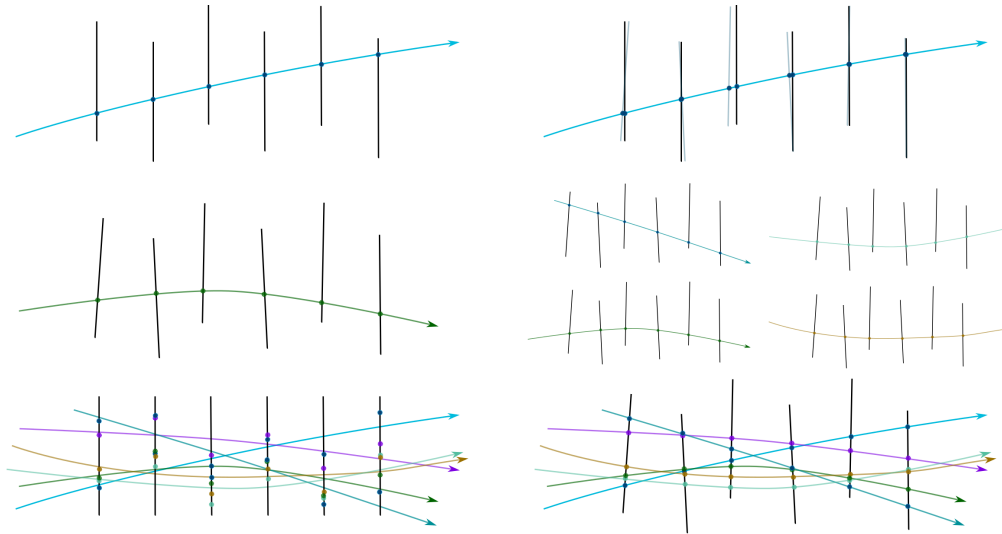


Figure 4.2: The alignment of a toy tracker, part 2.

In CMS, we have two alignment algorithms: Millepede-II [29] and HIP [21]. Millepede-II performs a simultaneous fit of all alignment parameters and all track parameters while HIP perform iterative fits of alignment parameters  $\mathbf{p}$  and track parameters  $\mathbf{q}_j$ .

We can align the large substructures and individual modules with respect to the locations and orientations of their substructures. The parameters to align large substructures include three coordinates  $X$ ,  $Y$ ,  $Z$  and three angles  $\alpha$ ,  $\beta$ ,  $\gamma$ . At the module level, we align positions and rotations with respect to the positions and angles of the corresponding large structure (Fig. 4.3). In addition, at the module level we align for surface deformations which are described by three parameters per sensor (Fig. 4.4).

It is important to use different sorts of tracks for the alignment. Cosmic tracks pass through the detector vertically and do not allow us to connect different subdetectors to one another. Collision tracks originate from the collision point and go in all directions. However, those tracks which cross TEC are all almost collinear and, therefore, it is difficult to measure  $z$ -coordinate of TEC modules with collision tracks only.

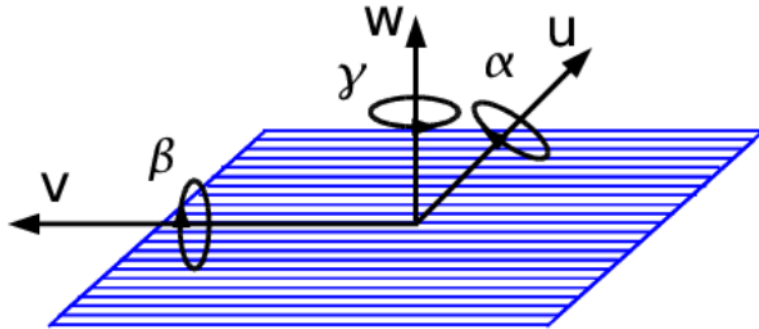


Figure 4.3: Alignment parameters.

It is necessary to align a part of the tracking system every time when we suspect a physical change in a location or an orientation this part. First of all, every time when CMS is taken out and placed back, all large structures need to be realigned. Also whenever a magnet is turned on and off, different parts of tracking system

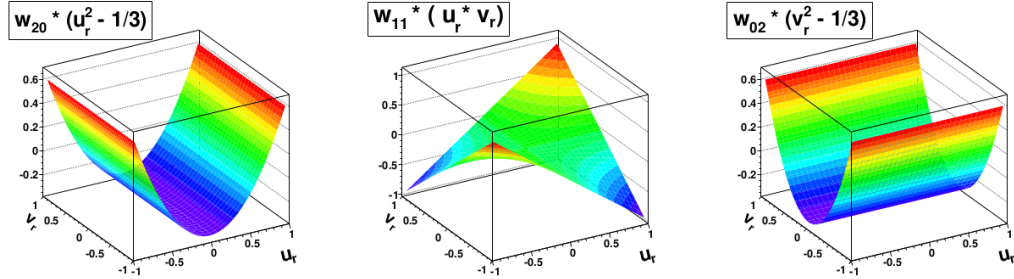


Figure 4.4: Surface deformations.

may shift with respect to one another. Pixel half barrels are not screwed firmly, they are moving along each other on rails and, therefore, need to be realigned every 15 minutes. Realignment on the module level is necessary when modules are replaced. Also, module deformations may change when temperature changes.

After the procedure of the tracking system alignment is performed, it is necessary to validate the results. Various tools of alignment validation are discussed in Chapter 4.2 using the example of the tracking system alignment based on the first Run II data.

## 4.2 Selected Results on Alignment of the Tracking System with 2015 Data

Different data-taking periods in 2015 include cosmic-ray data with the magnetic field  $B = 0\text{T}$  and  $B = 3.8\text{T}$ , and collision data at  $\sqrt{s} = 13\text{ TeV}$  center-of-mass energy with  $B = 0\text{T}$  and  $B = 3.8\text{T}$ . Different data-taking periods correspond to different detector geometries particularly due to changes of the magnetic field.

Alignment constants have been derived for each data-taking period using the data collected during that period. Alignments under study are the result of a combination of a global (Millepede-II) and local (HIP) fit approach. The results are obtained by different approaches of running the two algorithms in sequence. In each data-taking period, the starting point for the alignment fit is the alignment obtained in the previous data-taking period. In addition, the two algorithms run independently confirm each other.

The first alignment of the tracker, using  $B = 0\text{T}$  and  $B = 3.8\text{T}$  cosmic ray data, corrected for the shifts that took place since the end of Run I of the LHC. The pixels modules in particular were repaired during the shutdown, and the pixel subdetectors were also recentered within the tracker. The tracker geometry changed between the  $B = 3.8\text{T}$  cosmic ray data and the first collisions, recorded with the magnetic field off, primarily because the changing magnetic field causes movements in the tracker. These effects are apparent mostly in the pixels, and the alignment performed using  $B = 0\text{T}$  collisions and cosmic rays (taken in between collision-data runs) recovers the tracker performance. The tracker geometry changed again when the magnetic field was turned back on. New alignment constants are fitted for larger substructures of the pixel detector (BPIX half-barrels and FPIX half-cylinders) only. The changes, again produced by the changing

magnetic field, are recovered by this alignment.

Validation of tracking system alignment tools include geometry comparison tool (Ch. 4.2.1), validation using distribution of median residuals (Ch. 4.2.2), cosmic track splitting validation (Ch. 4.2.3), and primary vertex validation (Ch. 4.2.4). Full results of the first alignment with Run II data are available at [1].

### 4.2.1 Geometry Comparison

Geometry Comparison is a visualization of the module-position differences of two different tracker geometries. Each dot in Fig. 4.5 correspond to one module. Red dots correspond to the negative  $z$ -direction while black dots correspond to the positive one.

Comparison of Run II and Run I positions of the modules in the forward-pixel (FPIX) detector of the tracker is shown in Fig. 4.5. The positions are determined with the Millepede-II and HIP algorithms using cosmic ray data collected with  $B = 0\text{T}$  and  $B = 3.8\text{T}$  magnetic field in the solenoid. The difference  $\Delta z$  (Run II - Run I) as a functions of  $z$  (left) and  $\phi$  (right) in global coordinates. Modules in the endcap half-disks at the  $-z$  side are shown in red, modules in the half-disks at the  $+z$  side are shown in black. Four half-disks at the  $-z$  side (four clusters of red dots at the left plot) are displaced by  $-4.5\text{ mm}$  and  $-5.5\text{ mm}$ . Much smaller relative movements of up to  $200\text{ }\mu\text{m}$  are observed for the modules in the half-disks on the  $+z$  side (two clusters of black dots). Shifted half-disks are shown as four clusters of red dots at the left plot and as shifted parts at ( $\phi < -\pi/2, \phi > \pi/2$ ) and ( $-\pi/2 < \phi < \pi/2$ ) at the right plot.

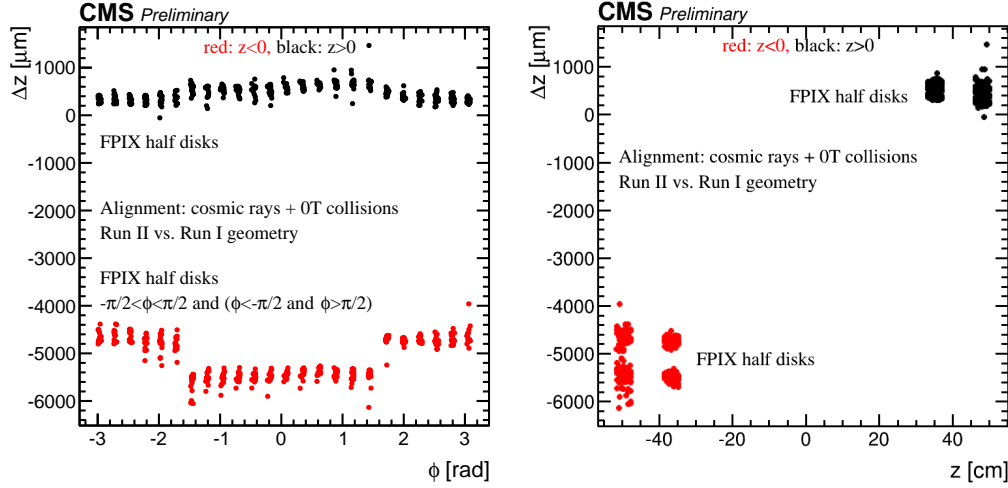


Figure 4.5: Comparison of Run II and Run I positions of the modules in the forward-pixel (FPIX) detector of the tracker, determined with the Millepede-II and HIP algorithms using cosmic ray data collected with  $B = 0\text{T}$  and  $B = 3.8\text{T}$  magnetic field in the solenoid. The difference  $\Delta z$  (Run II - Run I) as a functions of  $z$  (left) and  $\phi$  (right) in global coordinates. Modules in the endcap half-disks at the  $-z$  side are shown in red, modules in the half-disks at the  $+z$  side are shown in black.

#### 4.2.2 Distributions of Medians of Unbiased Track-Hit Residuals

Besides geometry comparison, we also have distributions of medians of unbiased track-hit residuals (DMR) validation tool. Each track is refitted using the alignment constants under consideration, and the hit prediction for each module is obtained from all of the other track hits. The median of the distribution of unbiased hit residuals is then taken for each module and is histogrammed. The width of this distribution of the medians of residuals (DMR) is a measure of the statistical precision of alignment results; deviations from zero indicate possible biases. The width also has an intrinsic component due to the limited number of tracks, meaning that distributions can only be compared if they are produced with the same number of tracks, as is the case within each set of plots here.

## CMS Preliminary

Alignment: cosmic rays + 0T collisions

Run II vs. Run I geometry, shift x 5

$> 4 \text{ mm}$

$2 \text{ mm} - 4 \text{ mm}$

$< 2 \text{ mm}$

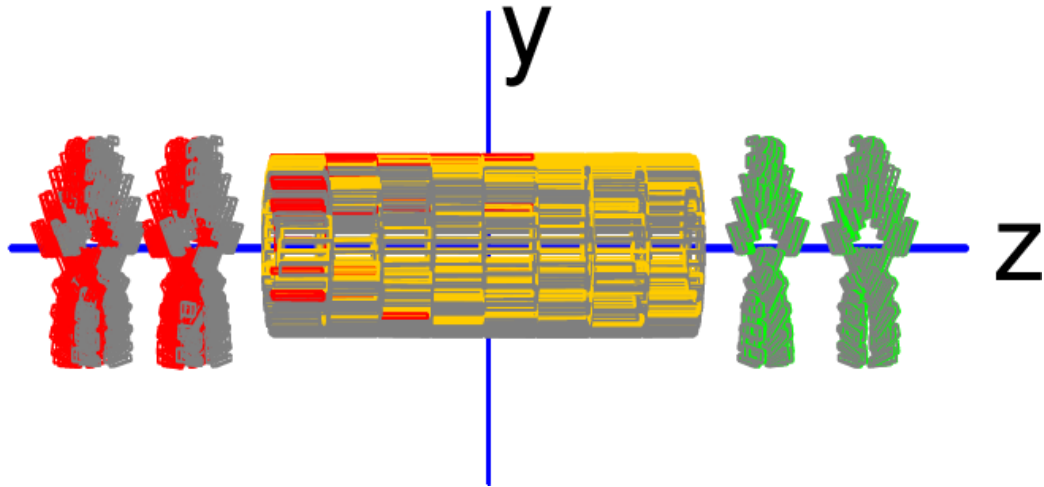


Figure 4.6: 3D comparison of Run II and Run I positions of the pixel modules of the tracker, determined with the Millepede-II and HIP algorithms using cosmic ray data collected with  $B = 0\text{T}$  and  $B = 3.8\text{T}$  magnetic field in the solenoid and  $B = 0\text{T}$  collision data at  $\sqrt{s} = 13 \text{ TeV}$ . The positions at the end of Run I are shown in gray. The module shifts between Run I and Run II are magnified by a factor of 5 for visualization, and the resulting positions are shown in red, yellow, or green, depending on the magnitude of the shift.

The DMRs in the transverse plane,  $d_{xy}$ , and in the longitudinal direction,  $d_z$ , are studied in bins of track azimuth  $\phi$  and pseudo-rapidity  $\eta$ . Random misalignments of the modules affect only the resolution of the unbiased track-vertex residual, increasing the width of the distributions, but without biasing their mean. Systematic movements of the modules will bias the distributions in a way that depends on the nature and size of the misalignment and the and of the selected tracks.

The DMRs are plotted for the local x-direction (Fig. 4.7, left) and for the local y-direction (Fig. 4.7, right) in the barrel pixel detector, using 2 million cosmic

ray tracks collected with the magnetic field at  $B = 3.8\text{T}$ . The blue line shows the Run I geometry, which is no longer valid for Run II data, primarily because of temperature changes and pixel re-centering and repair. The alignment shown in green was produced with the Millepede-II and HIP algorithms using  $B = 0\text{T}$  and  $B = 3.8\text{T}$  cosmic ray data. The RMS values, calculated using modules both inside and outside the plot range, show improvement over the Run I geometry by a factor of 10.

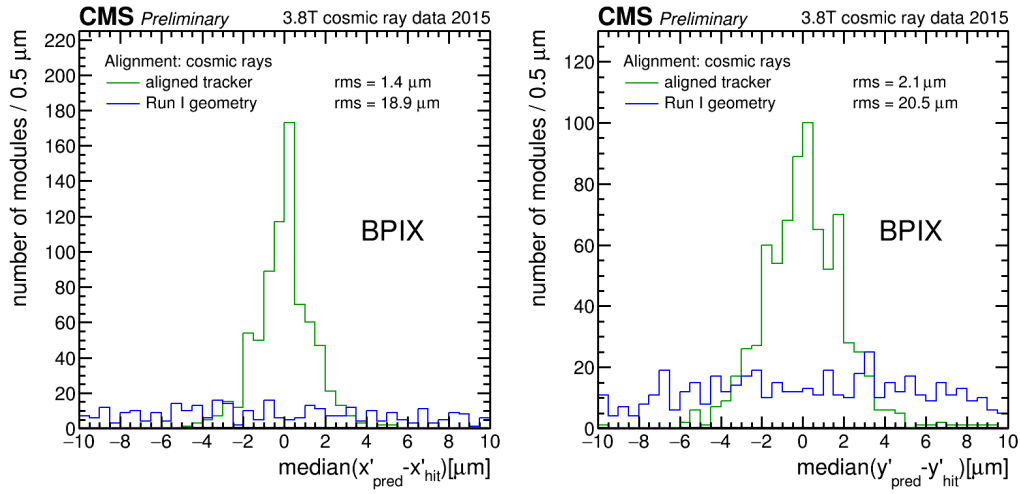


Figure 4.7: DMRs for the local  $x$ -direction (left) and for the local  $y$ -direction (right) in the barrel pixel detector, using 2 million cosmic ray tracks collected with the magnetic field at  $B = 3.8\text{T}$ . The blue line shows the Run I geometry. The alignment shown in green was produced with the Millepede-II and HIP algorithms using  $B = 0\text{T}$  and  $B = 3.8\text{T}$  cosmic ray data.

### 4.2.3 Cosmic Track Splitting Validation

Cosmic ray tracks are split in half at the hit closest to origin and refitted with the alignment constants under consideration. The differences in various track parameters between the two half-tracks are studied. The width of the distribution

measures the achieved alignment precision, while deviations from zero indicate possible biases.

Cosmic track splitting validation are shown in Fig. 4.8. The normalized differences between two halves of a cosmic track, split at the point of closest approach to the interaction region, in  $d_{xy}$  (Fig. 4.8, left), the  $xy$  distance between the track and the origin, and in  $d_z$  (right), the distance in the  $z$  direction between the track and the origin. The observed precision using the aligned geometry (green circles), produced with the Millepede-II and HIP algorithms using cosmic ray data at  $B = 0\text{T}$  and  $B = 3.8\text{T}$ , is a major improvement over the Run I geometry (blue empty squares). The precision comes close to that of the ideal Monte Carlo, illustrating that the tracker has almost reached its design spatial resolution.

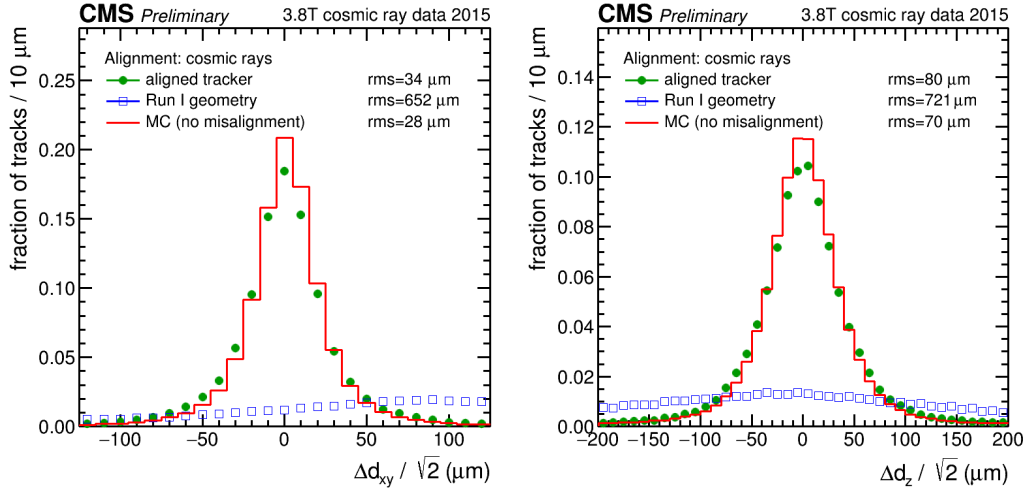


Figure 4.8: Cosmic track splitting validation. The normalized differences between two halves of a cosmic track, split at the point of closest approach to the interaction region, in  $d_{xy}$  (left), the  $xy$  distance between the track and the origin, and in  $d_z$  (right), the distance in the  $z$  direction between the track and the origin. Aligned geometry (green circles) is produced with the Millepede-II and HIP algorithms using cosmic ray data at  $B = 0\text{T}$  and  $B = 3.8\text{T}$ .

#### 4.2.4 Primary Vertex Validation

The resolution of the reconstructed vertex position is driven by the pixel detector since it is the closest detector to the interaction point and has the best hit resolution. The primary vertex residual method is based on the study the distance between the track and the vertex, the latter reconstructed without the track under scrutiny (unbiased track-vertex residual).

The distance in the transverse plane of the track at its closest approach to a refit unbiased primary vertex ( $d_{xy}$ , left and  $d_z$ , right) is studied in bins of track azimuth  $\phi$  using a sample of around 5.5M events collected by the CMS detector at zero magnetic field ( $B = 0\text{T}$ ) selected online through minimum bias triggers. The performance of a dedicated alignment achieved with the Millepede-II and HIP algorithms using cosmic ray data collected with  $B = 0\text{T}$  and  $B = 3.8\text{T}$  magnetic field and  $B = 0\text{T}$  collision data is compared to the one of a previous alignment reached during the commissioning phase with cosmic ray tracks at full magnetic field and to a detailed detector simulation with perfect alignment and calibration. The structures of the green curve indicate relative movements of the pixel half-barrels.

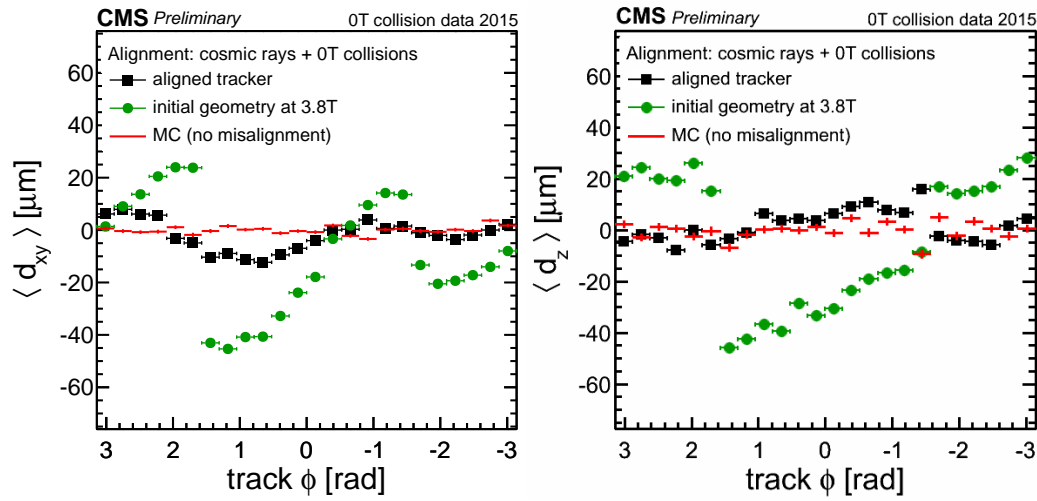


Figure 4.9: Primary Vertex Validation. The distance in the transverse plane of the track at its closest approach to a refit unbiased primary vertex ( $d_{xy}$ , left and  $d_z$ , right) in bins of track azimuth  $\phi$ . Validated with CMS data at  $B = 0\text{T}$ . Aligned with the Millepede-II and HIP algorithms using cosmic ray data collected with  $B = 0\text{T}$  and  $B = 3.8\text{T}$  magnetic field and  $B = 0\text{T}$  collision data.

# Chapter 5

## $W\gamma$ Cross Section Measurement

Place analysis outline here

# Bibliography

- [1] Cms tracker detector performance results 2015: Alignment. Available at: <https://twiki.cern.ch/twiki/bin/view/CMSPublic/TkAlignmentPerformance2015>.
- [2] ATLAS VW ( $V=W,Z \rightarrow jj$ ) using 4.6 fb $^{-1}$  of 7 TeV pp collisions JHEP 01 (2015) 049.
- [3] CMS TDR.
- [4] CMS 7 TeV Zg nunug.
- [5] CMS 8 TeV WW lnulnu.
- [6] Available at: <https://inspirehep.net/record/837874/plots>.
- [7] CMS VW ( $V=W,Z \rightarrow jj$ ) using 5.0 fb $^{-1}$  of 7 TeV pp collisions Eur.Phys.J. C73 (2013) 2283.
- [8] CMS WW using 4.9 fb $^{-1}$  of 7 TeV pp collisions Eur. Phys. J. C 73 (2013) 2610.
- [9] CMS WW using 19.4 fb $^{-1}$  of 8 TeV pp collisions Submitted to EPJC.
- [10] ATLAS Collaboration. Observation of a new particle in the search for the standard model higgs boson with the atlas detector at the lhc. *Phys. Lett. B*, 716(1):1–29, 2012. Available at: <https://arxiv.org/abs/1207.7214>.

- [11] CMS Collaboration. Observation of a new boson at a mass of 125 gev with cms experiment at the lhc. *Phys. Lett. B*, 716(1):30–61, 2012. Available at: <https://arxiv.org/abs/1207.7235>.
- [12] Wikipedia article. cross section (physics). Available at: [https://en.wikipedia.org/wiki/Cross\\_section\\_%28physics%29](https://en.wikipedia.org/wiki/Cross_section_%28physics%29).
- [13] Do Combination of  $W\gamma$ , WW, WZ and VW using 8.6 fb-1 of 2 TeV  $p\bar{p}$  collisions Phys.Lett. B718 (2012) 451-459.
- [14] website: <http://cds.cern.ch/record/1621583/files/>.
- [15] Available at: <https://twiki.cern.ch/twiki/bin/view/CMSPublic/LumiPublicResults>.
- [16] Available at: <http://cds.cern.ch/journal/CERNBulletin/2014/24/News%20Articles/170660>
- [17] L. Gray. *A measurement of the  $Z\gamma$  Cross Section and Limits on anomalous Gauge Couplings at  $\sqrt{s} = 7$  TeV Using CMS*. PhD thesis, University of Wisconsin - Madison, 8 2012.
- [18] D. Griffiths. *Introduction to Elementary Particles*. WILEY-VCH, 2008.
- [19] Martin Halzen. *Quarks and leptons*.
- [20] Hard scattering. Available at: <http://iopscience.iop.org/article/10.1088/0034-4885/70/1/R02>.
- [21] Hip algorithm.
- [22] LEP Combination of WW and single W using 0.7 fb-1 per experiment of  $e^+e^-$  collisions at WW pair production energies arXiv:1302.3415.
- [23] CERN brochure, <http://cds.cern.ch/record/1165534/files/CERN-Brochure-2009-003-Eng.pdf>.

- [24] Available at: <https://twiki.cern.ch/twiki/bin/view/CMSPublic/LumiPublicResults>.
- [25] LHC TDR.
- [26] Available at: <http://home.cern/topics/large-hadron-collider>.
- [27] Available at: [https://www-do.fnal.gov/results/publications\\_talks/thesis/snyder/html/nodis.html](https://www-do.fnal.gov/results/publications_talks/thesis/snyder/html/nodis.html).
- [28] MCFM generator.
- [29] Millepede ii algorithm.
- [30] Nasa website. Available at: <https://science.nasa.gov/astrophysics/focus-areas/what-is-dark-energy>.
- [31] Particle data group. Available at: [pdg.lbl.gov](http://pdg.lbl.gov).
- [32] <https://inspirehep.net/record/925379/files/PFT-09-001-pas.pdf>.
- [33] Schroeder Peskin. *Introduction to Quantum Field Theory*.
- [34] A. Pich. *The Standard Model of Electroweak Interactions*, 2007. Updated version of the lectures given at the 2006 European School of High Energy Physics (Aronsborg, Sweden, 18 June - 1 July 2006) and at the 4th CERN - CLAF School of High Energy Physics (Vina del Mar, Chile, 18 February - 3 March 2007). Available at: <https://arxiv.org/abs/0705.4264>.
- [35] 7TeV Wg ATLAS paper.
- [36] 7TeV Wg CMS paper.
- [37] ATLAS WW using 20.3 fb<sup>-1</sup> of 8 TeV pp collisions Submitted to JHEP.
- [38] website: [https://inspirehep.net/record/1235541/files/LHC\\_all.png](https://inspirehep.net/record/1235541/files/LHC_all.png).

- [39] website: <https://muon.files.wordpress.com/2014/01/cms-sigma-vs-e.png>.
- [40] PhD thesis. Senka's thesis, CMS Wg- $\tau$ munug, 7 TeV.
- [41] UNKNOWN [TEMPORARY]. Source of sm figure [temporary]. Available at:  
<http://www.isgtw.org/spotlight/go-particle-quest-first-cern-hackfest>.
- [42] aTGC paper, LEP parametrization.
- [43] LO (1969) theory paper.
- [44] NLO theory paper.
- [45] NNLO theory paper.
- [46] Available at: <https://twiki.cern.ch/twiki/bin/view/CMSPublic/PhysicsResultsSMPaTGC#>